Nonlinear Dynamics and Modeling of Various Wooden Toys with Impact and Friction

R. I. LEINE
D. H. VAN CAMPEN
Department of Mechanical Engineering, Eindhoven University of Technology, P.O. Box 513, 5600 MB Eindhoven, The Netherlands

CH. GLOCKER
Institute of Mechanical Systems, Center of Mechanics, ETH Zentrum, CH-8092 Zürich, Switzerland

(Received 20 April 2001; accepted 6 August 2001)

Abstract: In this paper, we study bifurcations in systems with impact and friction, modeled with a rigid multibody approach. Knowledge from the field of nonlinear dynamics is therefore combined with theory from the field of non-smooth mechanics. We study the nonlinear dynamics of three commercial wooden toys. The toys show complex dynamical behavior but can be studied with one-dimensional maps, which allows for a thorough analysis of the bifurcations.

Key Words: Bifurcations, multibody dynamics, linear complementarity problem, contact

1. INTRODUCTION

The aim of this paper is to study bifurcations in systems with impact and friction, modeled with a rigid multibody approach. Knowledge from the field of nonlinear dynamics is therefore combined with theory from the field of non-smooth mechanics. We study the nonlinear dynamics of three commercial wooden toys. The toys show complex dynamical behavior but can be studied with one-dimensional maps, which allows for a thorough analysis of the bifurcations.

Impact with friction can be present between two or more bodies of a system. Periodic impact of colliding bodies or rubbing of bodies in contact can be highly detrimental to mechanical systems, such as rattling in gear boxes and stick–slip phenomena in cutting processes. On the other hand, many mechanical systems rely on impulsive and stick–slip processes to perform their intended functions (a hammer drill, for instance). Modeling of systems with impact and friction has received increasingly more attention in the literature, because of the need to predict, control or avoid vibrations in systems with impact and friction. The global dynamics of the system is therefore of interest, and not the tribological

Journal of Vibration and Control, **9**: 25–78, 2003
DOI: 10.1177/107754603030741

processes of the contact surface, which allows simplified contact models. Mainly, two different approaches exist to model systems with unilateral contacts.

A vast majority of the existing literature approaches the problem by using compliant impact models (a stiff spring) and a smoothed friction characteristic; see, for example, Begley and Virgin (1997), Canudas de Wit et al. (1995), Natsiavas and Gonzalez (1992), Van de Vrande et al. (1999), and Wiercigroch (1996). These regularization methods have the disadvantage of yielding a set of stiff ordinary differential equations (ODEs), which are expensive to solve. Moreover, it is not clear how to determine the dissipation parameters of the contact unambiguously (Brogliato, 1999).

A second way to deal with systems with impact and friction is the rigid multibody approach (Brogliato, 1999; Glocker, 1995; Pfeiffer and Glocker, 1996). This approach models the system as a set of rigid bodies, interconnected by joints, springs, dashpots and nonlinear couplings. Wave effects within a body are neglected in the rigid multibody approach. Impact between the bodies and stick–slip transitions of bodies in contact are considered to be instantaneous and are described by contact laws. Newton's impact law or Poisson's law are usually taken as impact law in the normal direction. Newton's law relates post-impact velocities to pre-impact velocity with a restitution coefficient. Poisson's law treats the impact as a compression and expansion phase and relates the impulse stored during compression to the impulse released in the expansion phase with a restitution coefficient. The Amontons–Coulomb law, in which the friction force is in the opposite direction to the relative velocity and proportional to the normal force, is usually taken as contact law in a tangential direction. The restitution coefficient and friction coefficient can be measured in a straightforward manner from simple experiments (Beitelschmidt, 1999). The rigid multibody approach avoids stiff differential equations and is therefore more economical than regularization methods. This advantage is at the cost of a more complex mathematical formulation. Multibody systems with multiple contacts bring forth a combinatorial problem of large dimensions. If the state in one contact changes, for example from contact to detachment or from stick to slip, all other contacts are also influenced, which makes a search for a new set of contact configurations necessary. A rigorous way to perform the search for a new contact configuration is to formulate the problem as a linear complementarity problem (LCP), for which standard numerical solvers are available. If the transition times of impact and stick–slip transitions are small in comparison with the times between transitions, and if wave effects can be neglected, then the rigid multibody approach can be expected to give good results. Regularization methods, together with more sophisticated tribological contact models, might be more recommendable when the transition times are relatively large. Wave effects have to be studied by partial differential equations or their discretizations by finite element methods. We focus on the rigid multibody approach in the following, as for most systems the transition times are indeed very short. The rigid multibody approach then provides an economical and practical method to obtain the evolution in time of the generalized coordinates of the system by means of numerical integration.

As a second analysis step, we might be interested not only in time integration, but also in studying stable and unstable equilibria and periodic solutions and their dependences on parameters of the system. Nonlinear analysis methods, such as shooting and continuation techniques (also called path-following techniques), have been developed in the field of nonlinear dynamics, to find periodic solutions and to follow branches of periodic solutions for varying system parameters. A branch of periodic solutions can fold or bifurcate at critical

values of the system parameter. This qualitative change is called 'bifurcation'. Bifurcations are essential for understanding why vibrations are created, disappear or change qualitatively when a design variable of the system is varied. The theory of bifurcations is therefore important for the analysis of the dynamical behavior and design of systems.

Unilateral contact laws, as used in the rigid multibody approach, lead to non-smooth mathematical models due to their set-valued nature. Bifurcations in smooth systems are well understood (Guckenheimer and Holmes, 1983) but little is known about bifurcations in non-smooth systems (Leine, 2000). The literature on bifurcations in non-smooth mechanical systems seems to be divided into two groups:

1. Bifurcations in systems with *friction*, which belong to the class of Filippov systems. The literature on this topic is vast; for instance, Dankowicz and Nordmark (2000), Galvanetto and Knudsen (1997), Leine and Van Campen (1999), Leine and Van Campen (2000), Popp et al. (1995), Van de Vrande et al. (1999), Wiercigroch (1996), and Yoshitake and Sueoka (2000). A general theory for bifurcations in Filippov systems is not available but attempts to explore in that direction have been made (di Bernardo et al., 1999; Leine et al., 2000; Leine, 2000).
2. Bifurcations in systems with *impact* (Foale and Bishop, 1994; Ivanov, 1996; Meijaard, 1996; Nordmark, 1997; Peterka, 1996). The impacts are almost always considered to be frictionless and the systems very often contain only a single contact.

There is little literature available on bifurcations in systems with multiple contacts with combined friction and impact. An impact oscillator with friction has been studied in Blazejczyk-Okolewska and Kapitaniak (1996) but the impact and friction are in different contact points for this system and the contact problem is therefore decoupled.

In the present paper, we study bifurcations in geometrically simple dynamical systems with multiple contacts with impact and friction occurring in the same contact points. The systems are mechanical wooden toys, which show limit cycling behavior, and can very well be modeled with the rigid multibody approach. Although the toys might look simple at first sight, their dynamics is rather complicated and governed by non-standard bifurcations. The rigid multibody approach is briefly discussed in Section 3 after introducing the LCP in Section 2. The modeling and results obtained from the nonlinear analysis of the woodpecker toy, the tumbling toy and the waddling duck are discussed in Sections 4–6. Conclusions are given in Section 7.

2. THE LINEAR COMPLEMENTARITY PROBLEM

The LCP (Cottle and Dantzig, 1968) is a set of linear equations

$$\mathbf{y} = \mathbf{A}\mathbf{x} + \mathbf{b} \tag{1}$$

subjected to the complementarity conditions

$$\mathbf{y} \geq \mathbf{0}, \quad \mathbf{x} \geq \mathbf{0}, \quad \mathbf{y}^{\mathrm{T}}\mathbf{x} = 0, \tag{2}$$

for which the vectors $\mathbf{x}$ and $\mathbf{y}$ have to be solved for given $\mathbf{A}$ and $\mathbf{b}$. An LCP can have a unique solution, multiple solutions or no solution at all. All existing solutions can be found with enumerative methods, which treat the problem by a combinatorial evolution of the complementarity condition $x_i y_i = 0$. From the complementarity condition it follows that when $x_i > 0$, then $y_i = 0$, and vice versa. An LCP of dimension n therefore provides 2^n different combinations of n variables, which are allowed to be greater than zero at the same time. For large dimensions, enumerative methods become numerically expensive since 2^n grows very rapidly. A more efficient algorithm is the complementary pivot algorithm, usually referred to as Lemke's algorithm. A drawback of Lemke's algorithm is that it is not guaranteed to find a solution for arbitrary $\mathbf{A}$ (convergence is guaranteed when $\mathbf{A}$ is a P-matrix).

3. MATHEMATICAL MODELING OF IMPACT WITH FRICTION

In this section we briefly review a mathematical theory for the dynamics of rigid bodies with the Poisson–Coulomb impact formulated in Glocker (1995), and Pfeiffer and Glocker (1996). The current formulation is slightly different from Glocker (1995) and Pfeiffer and Glocker (1996) as it contains some ideas from the work of Roßmann (1998). A tangential restitution coefficient is not taken into account in the present formulation.

We introduce four contact sets, which describe the kinematic state of the contact points:

$$\begin{aligned} I_G &= \{1, 2, \ldots, n_G\} \\ I_S &= \{i \in I_G \mid g_{Ni} = 0\} \quad \text{with } n_S \text{ elements} \\ I_N &= \{i \in I_S \mid \dot{g}_{Ni} = 0\} \quad \text{with } n_N \text{ elements} \\ I_H &= \{i \in I_N \mid \dot{g}_{Ti} = 0\} \quad \text{with } n_H \text{ elements,} \end{aligned} \tag{3}$$

where g_{Ni} and $\dot{g}_{Ti}$ denote the normal contact distance and tangential relative velocity of contact point i. The set I_G consists of n_G indices of all contact points. I_S contains the n_S indices of the constraints with vanishing normal distance but arbitrary relative velocity. In the set, I_N are the n_N indices of the potentially active normal constraints, which fulfill the necessary conditions for continuous contact (vanishing normal distance and no relative velocity in the normal direction). I_N contains, therefore, all indices of slipping or sticking contacts. The n_H elements of the set I_H correspond to the potentially active constraints in the tangential direction (sticking). The sets I_S, I_N, and I_H are not constant, because the contact configuration of the dynamical system changes with time due to stick–slip transitions, impact and contact loss.

The dynamics of a multibody system can be expressed by the equation of motion

$$\mathbf{M}(t, \mathbf{q})\ddot{\mathbf{q}} - \mathbf{h}(t, \mathbf{q}, \dot{\mathbf{q}}) - \sum_{i \in I_S} (\mathbf{w}_N \lambda_N + \mathbf{w}_T \lambda_T)_i = \mathbf{0}, \tag{4}$$

where $\mathbf{M}$ is the symmetric mass matrix, $\mathbf{q}$ is the vector with generalized coordinates, $\mathbf{h}$ is the vector with all smooth elastic, gyroscopic and dissipating generalized forces and $\boldsymbol{\lambda}_N$ and $\boldsymbol{\lambda}_T$ are the vectors with normal and tangential contact forces. The vectors $\mathbf{w}_N$ and $\mathbf{w}_T$ are the

normal and tangential force directions. The contact forces can be looked upon as Lagrangian multipliers. In the following subsection, we formulate the contact problem for stick–slip transitions and detachment as an LCP on the acceleration level. The Coulomb friction law is applied for the tangential constraint. Impact will be treated separately, because impacts induce velocity jumps, which have to be calculated on the velocity level. The Poisson impact law is applied, consisting of a compression phase, during which impulse is stored, and an expansion phase, during which part of the stored impulse is released. The contact problem is formulated in Subsections 3.2 and 3.3 as two subsequent LCPs for the compression and expansion phase.

3.1. Stick–slip Transitions and Detachment

For the description of stick–slip transitions and detachment, we formulate the equation of motion (4) and the constraints on the acceleration level:

$$\mathbf{M}\ddot{\mathbf{q}} - \mathbf{h} - \left[\left(\mathbf{W}_N + \mathbf{W}_G\bar{\bar{\boldsymbol{\mu}}}_G\right)\mathbf{W}_H\right]\begin{bmatrix}\boldsymbol{\lambda}_N\\ \boldsymbol{\lambda}_H\end{bmatrix} = \mathbf{0} \tag{5}$$

$$\begin{bmatrix}\ddot{\mathbf{g}}_N\\ \ddot{\mathbf{g}}_H\end{bmatrix} = \begin{bmatrix}\mathbf{W}_N^{\mathrm{T}}\\ \mathbf{W}_H^{\mathrm{T}}\end{bmatrix}\ddot{\mathbf{q}} + \begin{bmatrix}\bar{\mathbf{w}}_N\\ \bar{\mathbf{w}}_H\end{bmatrix} \quad \in \mathbb{R}^{n_N+n_H}\,. \tag{6}$$

The vectors $\boldsymbol{\lambda}_N \in \mathbb{R}^{n_N}$ and $\ddot{\mathbf{g}}_N \in \mathbb{R}^{n_N}$ contain the contact forces and accelerations of the closed contacts $\in I_N$ in the normal directions, where $\boldsymbol{\lambda}_H \in \mathbb{R}^{n_H}$ and $\ddot{\mathbf{g}}_H \in \mathbb{R}^{n_H}$ consist of the tangential forces and accelerations of the potentially sticking contacts $\in I_H$. The friction forces of the sliding constraints are already expressed by their corresponding normal forces $\boldsymbol{\lambda}_G = \bar{\bar{\boldsymbol{\mu}}}_G\boldsymbol{\lambda}_N$ and occur in equation (5) by the matrix expression $\mathbf{W}_G\bar{\bar{\boldsymbol{\mu}}}_G$, where $\bar{\bar{\boldsymbol{\mu}}}_G$ is the diagonal matrix of friction coefficients. The normal and tangential contact accelerations are expressed in the generalized coordinates in equation (6). The remaining elements of I_S are not taken into account in equation (5) because they correspond to collisions and must be treated separately (see Subsections 3.2 and 3.3).

Each closed contact $i \in I_N$ is characterized by a vanishing contact distance g_{Ni} and normal relative velocity $\dot{g}_{Ni}$. Under the assumption of impenetrability $g_{Ni} \geq 0$, only two situations may occur:

$$\begin{aligned}&\ddot{g}_{Ni} = 0 \wedge \lambda_{Ni} \geq 0 \quad \text{contact is maintained,}\\ &\ddot{g}_{Ni} > 0 \wedge \lambda_{Ni} = 0 \quad \text{detachment.}\end{aligned} \tag{7}$$

From equation (7) we see that the normal contact law shows a complementary behavior; the product of the contact force and acceleration is always zero

$$\ddot{g}_{Ni}\,\lambda_{Ni} = 0, \quad i \in I_N\,. \tag{8}$$

The complementary behavior of the normal contact law is depicted in Figure 1(a) and shows a corner of admissible combinations of $\ddot{g}_{Ni}$ and λ_{Ni}. Unilateral laws of this type (showing

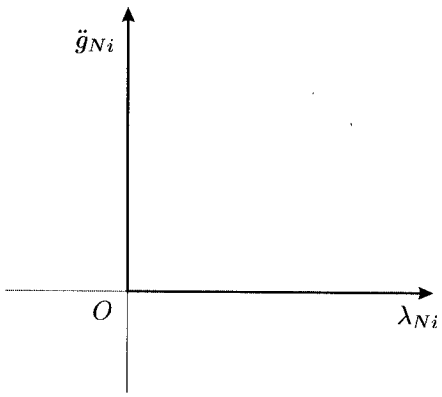

(a) normal direction

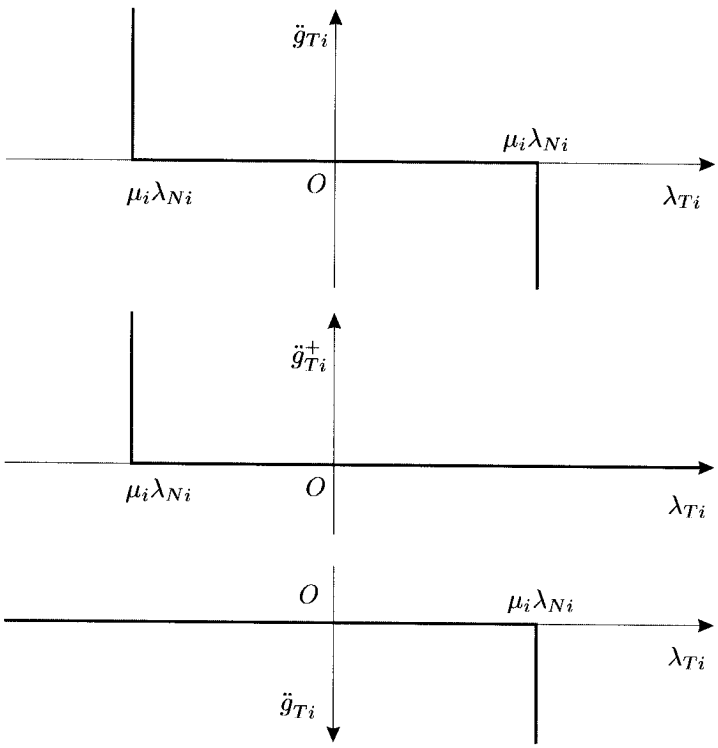

(b) tangential direction

Figure 1. Complementarity of contacts.

one corner) lead, together with the equations of motion, to an LCP as we see in the remainder of this section.

With respect to the tangential direction, we need to express the Coulomb friction law in similar unilateral primitives. For a closed contact $i \in I_N$, with friction coefficient μ_i, the following three cases are possible:

$$\begin{aligned} \dot{g}_{Ti} = 0 \quad &\Rightarrow \quad |\lambda_{Ti}| \leq \mu_i \lambda_{Ni} \quad \text{sticking} \\ \dot{g}_{Ti} < 0 \quad &\Rightarrow \quad \lambda_{Ti} = +\mu_i \lambda_{Ni} \quad \text{negative sliding} \quad i \in I_N . \\ \dot{g}_{Ti} > 0 \quad &\Rightarrow \quad \lambda_{Ti} = -\mu_i \lambda_{Ni} \quad \text{positive sliding} \end{aligned} \tag{9}$$

To determine the tangential contact force during sticking, we formulate unilateral laws for sticking contacts. For a closed sticking contact $i \in I_H$, the following three cases are possible:

$$\begin{aligned} \ddot{g}_{Ti} = 0 \quad &\Rightarrow \quad |\lambda_{Ti}| \leq \mu_i \lambda_{Ni} \quad \text{remains sticking} \\ \ddot{g}_{Ti} < 0 \quad &\Rightarrow \quad \lambda_{Ti} = +\mu_i \lambda_{Ni} \quad \text{commences negative sliding} \quad i \in I_H . \\ \ddot{g}_{Ti} > 0 \quad &\Rightarrow \quad \lambda_{Ti} = -\mu_i \lambda_{Ni} \quad \text{commences positive sliding} \end{aligned} \tag{10}$$

The tangential contact law is shown in the upper part of Figure 1(b) and shows two corners. The tangential contact law must therefore be decomposed into two separate unilateral primitives, which is shown in the lower part of Figure 1(b). The decomposition involves the splitting of $\ddot{g}_{Ti}$ into positive and negative parts:

$$\ddot{g}_{Ti}^{+} = \frac{1}{2}(|\ddot{g}_{Ti}| + \ddot{g}_{Ti}), \quad \ddot{g}_{Ti}^{-} = \frac{1}{2}(|\ddot{g}_{Ti}| - \ddot{g}_{Ti}), \quad \ddot{g}_{Ti} = \ddot{g}_{Ti}^{+} - \ddot{g}_{Ti}^{-}. \tag{11}$$

The positive and negative parts of the accelerations are gathered in the vectors $\ddot{\mathbf{g}}_H^{+} = \{\ddot{g}_{Ti}^{+}\}$ and $\ddot{\mathbf{g}}_H^{-} = \{\ddot{g}_{Ti}^{-}\}$, $i \in I_H$. Furthermore, we need to define the friction saturations $\boldsymbol{\lambda}_{H0}^{(+)}$ and $\boldsymbol{\lambda}_{H0}^{(-)}$, i.e. the differences in force on the horizontal axes relative to the origins of the two corners:

$$\boldsymbol{\lambda}_{H0}^{(+)} = \bar{\bar{\boldsymbol{\mu}}}_H \boldsymbol{\lambda}_N + \boldsymbol{\lambda}_H \tag{12}$$

$$\boldsymbol{\lambda}_{H0}^{(-)} = \bar{\bar{\boldsymbol{\mu}}}_H \boldsymbol{\lambda}_N - \boldsymbol{\lambda}_H . \tag{13}$$

Adding equations (12) and (13) gives the relation

$$\boldsymbol{\lambda}_{H0}^{(+)} = 2\bar{\bar{\boldsymbol{\mu}}}_H \boldsymbol{\lambda}_N - \boldsymbol{\lambda}_{H0}^{(-)}, \tag{14}$$

which will be of use later. The friction saturations $\boldsymbol{\lambda}_{H0}^{(+)}$ and $\boldsymbol{\lambda}_{H0}^{(-)}$ are complementary to the acceleration vectors $\ddot{\mathbf{g}}_H^{+}$ and $\ddot{\mathbf{g}}_H^{-}$, and can therefore be used to setup an LCP on the acceleration

level for the tangential contact problem. Equation (13) is substituted in the equation of motion (5)

$$\begin{aligned}\ddot{\mathbf{q}} &= \mathbf{M}^{-1}\mathbf{h} + \mathbf{M}^{-1}(\mathbf{W}_N + \mathbf{W}_G\bar{\bar{\boldsymbol{\mu}}}_G)\boldsymbol{\lambda}_N + \mathbf{M}^{-1}\mathbf{W}_H\boldsymbol{\lambda}_H \\ &= \mathbf{M}^{-1}\mathbf{h} + \mathbf{M}^{-1}(\mathbf{W}_N + \mathbf{W}_G\bar{\bar{\boldsymbol{\mu}}}_G + \mathbf{W}_H\bar{\bar{\boldsymbol{\mu}}}_H)\boldsymbol{\lambda}_N - \mathbf{M}^{-1}\mathbf{W}_H\boldsymbol{\lambda}_{H0}^{(-)}. \end{aligned} \tag{15}$$

The acceleration $\ddot{\mathbf{q}}$ is subsequently substituted in the first line of the contact equations (6), which gives

$$\begin{aligned}\ddot{\mathbf{g}}_N &= \mathbf{W}_N^{\mathrm{T}}\mathbf{M}^{-1}\mathbf{h} + \mathbf{W}_N^{\mathrm{T}}\mathbf{M}^{-1}\underbrace{(\mathbf{W}_N + \mathbf{W}_G\bar{\bar{\boldsymbol{\mu}}}_G + \mathbf{W}_H\bar{\bar{\boldsymbol{\mu}}}_H)}_{\mathbf{W}_Q}\boldsymbol{\lambda}_N \\ &\quad - \mathbf{W}_N^{\mathrm{T}}\mathbf{M}^{-1}\mathbf{W}_H\boldsymbol{\lambda}_{H0}^{(-)} + \bar{\mathbf{w}}_N. \end{aligned} \tag{16}$$

Similarly, an expression for $\ddot{\mathbf{g}}_H^-$ is obtained, substituting the second line of equation (6)

$$\ddot{\mathbf{g}}_H^- = -\mathbf{W}_H^{\mathrm{T}}\mathbf{M}^{-1}\mathbf{h} - \mathbf{W}_H^{\mathrm{T}}\mathbf{M}^{-1}\mathbf{W}_Q\boldsymbol{\lambda}_N + \mathbf{W}_H^{\mathrm{T}}\mathbf{M}^{-1}\mathbf{W}_H\boldsymbol{\lambda}_{H0}^{(-)} + \ddot{\mathbf{g}}_H^+ - \bar{\mathbf{w}}_H, \tag{17}$$

where the relation $\ddot{\mathbf{g}}_H = \ddot{\mathbf{g}}_H^+ - \ddot{\mathbf{g}}_H^-$ and the abbreviation $\mathbf{W}_Q$ (16) are used. Equations (16), (17) and (14) form together an LCP on the acceleration level for the tangential contact problem:

$$\underbrace{\begin{bmatrix}\ddot{\mathbf{g}}_N \\ \ddot{\mathbf{g}}_H^- \\ \boldsymbol{\lambda}_{H0}^{(+)}\end{bmatrix}}_{\mathbf{y}} = \underbrace{\begin{bmatrix}\mathbf{W}_N^{\mathrm{T}}\mathbf{M}^{-1}\mathbf{W}_Q & -\mathbf{W}_N^{\mathrm{T}}\mathbf{M}^{-1}\mathbf{W}_H & \mathbf{0}_{n_N\times n_H} \\ -\mathbf{W}_H^{\mathrm{T}}\mathbf{M}^{-1}\mathbf{W}_Q & \mathbf{W}_H^{\mathrm{T}}\mathbf{M}^{-1}\mathbf{W}_H & \mathbf{E}_{n_H\times n_H} \\ 2\bar{\bar{\boldsymbol{\mu}}}_H & -\mathbf{E}_{n_H\times n_H} & \mathbf{0}_{n_H\times n_H}\end{bmatrix}}_{\mathbf{A}} \underbrace{\begin{bmatrix}\boldsymbol{\lambda}_N \\ \boldsymbol{\lambda}_{H0}^{(-)} \\ \ddot{\mathbf{g}}_H^+\end{bmatrix}}_{\mathbf{x}} + \underbrace{\begin{bmatrix}\mathbf{W}_N^{\mathrm{T}}\mathbf{M}^{-1}\mathbf{h} + \bar{\mathbf{w}}_N \\ -\mathbf{W}_H^{\mathrm{T}}\mathbf{M}^{-1}\mathbf{h} - \bar{\mathbf{w}}_H \\ \mathbf{0}_{n_H\times 1}\end{bmatrix}}_{\mathbf{b}}. \tag{18}$$

3.2. Compression Phase of Impact

The LCP for the compression phase using the Poisson impact law is formulated in this subsection. The way the LCP will be setup is very similar to the formulation of the tangential

contact problem in the previous subsection, although the LCP is now formulated on the velocity level instead of the acceleration level because we are interested in jumps in the velocities due to an impact. For the formulation of the impact equations, we take into account all active unilateral constraints, which means constraints that are elements of I_S. All sliding and sticking contacts, as well as impact contacts are taken into account. We start again with the equation of motion

$$\mathbf{M}\ddot{\mathbf{q}} - \mathbf{h} - [\mathbf{W}_N \quad \mathbf{W}_T] \begin{bmatrix} \boldsymbol{\lambda}_N \\ \boldsymbol{\lambda}_T \end{bmatrix} = \mathbf{0}, \tag{19}$$

where $\boldsymbol{\lambda}_T \in \mathbb{R}^{ns}$ is the contact force in the tangential direction for both slipping and sticking contacts. The compression phase is assumed to begin at time t_A and to end at a time t_C. The time difference $t_C - t_A$ is assumed to be "infinitely small"[1] in the rigid multibody approach. The equation of motion is integrated over the compression phase

$$\mathbf{M}(\dot{\mathbf{q}}_C - \dot{\mathbf{q}}_A) = [\mathbf{W}_N \quad \mathbf{W}_T] \begin{bmatrix} \boldsymbol{\lambda}_{NC} \\ \boldsymbol{\lambda}_{TC} \end{bmatrix}, \tag{20}$$

which yields the velocity jump over the compression phase $\dot{\mathbf{q}}(t_C) - \dot{\mathbf{q}}(t_A) = \dot{\mathbf{q}}_C - \dot{\mathbf{q}}_A$ as a function of the impulses $\boldsymbol{\Lambda}_{NC}$ and $\boldsymbol{\Lambda}_{TC}$ in the normal and tangential directions defined by

$$\Lambda_{NCi} = \lim_{t_C \to t_A} \int_{t_A}^{t_C} \lambda_{Ni}\, \mathrm{d}t, \quad \Lambda_{TCi} = \lim_{t_C \to t_A} \int_{t_A}^{t_C} \lambda_{Ti}\, \mathrm{d}t, \quad i \in I_S. \tag{21}$$

Due to the unilateral characteristic of the contact constraint, only non-negative normal contact forces are possible, $\lambda_{Ni} \geq 0$, which results in non-negative values of the normal impulses $\Lambda_{NCi} \geq 0$. At the end of the compression phase, the approaching process of the bodies has to be completed. Thus, negative values of the contact velocities are forbidden, $\dot{g}_{NCi} \geq 0$. If an impulse is transferred ($\Lambda_{NCi} > 0$), then the corresponding contact participates in the impact and the end of the compression phase is given by $\dot{g}_{NCi} = 0$. If no impulse is transferred ($\Lambda_{NCi} = 0$), then the corresponding constraint is superfluous and we allow velocities $\dot{g}_{NCi} \geq 0$. The impact law in the normal direction for compression is therefore expressed by the complementarity condition

$$\Lambda_{NCi} \geq 0, \quad \dot{g}_{NCi} \geq 0, \quad \Lambda_{NCi}\, \dot{g}_{NCi} = 0; \quad i \in I_S. \tag{22}$$

We now have to formulate an impact law in the tangential direction during compression. Possible stick–slip transitions during the collision with reversed sliding prevent an analytical integration of the Coulomb friction law (10) over the impact time interval. However, we state the tangential impact law for compression as

$$\begin{aligned}
\dot{g}_{TCi} = 0 \quad &\Rightarrow \quad |\Lambda_{TCi}| \leq \mu_i \Lambda_{NCi} \quad \text{sticking} \\
\dot{g}_{TCi} < 0 \quad &\Rightarrow \quad \Lambda_{TCi} = +\mu_i \Lambda_{NCi} \quad \text{negative sliding} \qquad i \in I_S. \\
\dot{g}_{TCi} > 0 \quad &\Rightarrow \quad \Lambda_{TCi} = -\mu_i \Lambda_{NCi} \quad \text{positive sliding}
\end{aligned} \tag{23}$$

with the remark that equation (23) coincides with the Coulomb friction law (10) in the cases of continuous sliding during compression and of arbitrary transitions to sticking at the end of compression. Only events of reversed sliding or transitions from sticking to sliding with a sliding phase at the end of compression are different from the Coulomb law (Glocker, 1995; Moreau, 1988; Pfeiffer and Glocker, 1996).

The contact velocities in the normal and tangential directions can be expressed in the generalized velocities

$$\begin{bmatrix} \dot{\mathbf{g}}_N \\ \dot{\mathbf{g}}_T \end{bmatrix} = \begin{bmatrix} \mathbf{W}_N^{\mathrm{T}} \\ \mathbf{W}_T^{\mathrm{T}} \end{bmatrix} \dot{\mathbf{q}} + \begin{bmatrix} \hat{\mathbf{w}}_N \\ \hat{\mathbf{w}}_T \end{bmatrix} \quad \in \mathbb{R}^{2n_S} . \tag{24}$$

Evaluating the contact velocities (24) at t_C and t_A gives

$$\begin{bmatrix} \dot{\mathbf{g}}_{NC} \\ \dot{\mathbf{g}}_{TC} \end{bmatrix} = \begin{bmatrix} \mathbf{W}_N^{\mathrm{T}} \\ \mathbf{W}_T^{\mathrm{T}} \end{bmatrix} (\dot{\mathbf{q}}_C - \dot{\mathbf{q}}_A) + \begin{bmatrix} \dot{\mathbf{g}}_{NA} \\ \dot{\mathbf{g}}_{TA} \end{bmatrix} \quad \in \mathbb{R}^{2n_S} . \tag{25}$$

Completely analogous to the previous subsection, we split the friction characteristic into two corners with the friction saturation impulses $\mathbf{\Lambda}_{T0C}^{(+)}$ and $\mathbf{\Lambda}_{T0C}^{(-)}$

$$\mathbf{\Lambda}_{T0C}^{(+)} = \bar{\boldsymbol{\mu}}_S \mathbf{\Lambda}_{NC} + \mathbf{\Lambda}_{TC} \tag{26}$$

$$\mathbf{\Lambda}_{T0C}^{(-)} = \bar{\boldsymbol{\mu}}_S \mathbf{\Lambda}_{NC} - \mathbf{\Lambda}_{TC} \tag{27}$$

and with the decomposition of $\dot{\mathbf{g}}_{TC}$

$$\dot{\mathbf{g}}_{TC} = \dot{\mathbf{g}}_{TC}^{+} - \dot{\mathbf{g}}_{TC}^{-} . \tag{28}$$

Equation (27) is substituted in the impulse equation (20)

$$\mathbf{M}(\dot{\mathbf{q}}_C - \dot{\mathbf{q}}_A) = \mathbf{W}_N \mathbf{\Lambda}_{NC} + \mathbf{W}_T \left(\bar{\boldsymbol{\mu}}_S \mathbf{\Lambda}_{NC} - \mathbf{\Lambda}_{T0C}^{(-)} \right) . \tag{29}$$

The velocity jump $\dot{\mathbf{q}}_C - \dot{\mathbf{q}}_A$ is subsequently substituted in the contact velocities (25), which gives

$$\dot{\mathbf{g}}_{NC} = \mathbf{W}_N^{\mathrm{T}} \mathbf{M}^{-1} \underbrace{(\mathbf{W}_N + \mathbf{W}_T \bar{\boldsymbol{\mu}}_S)}_{\mathbf{W}_{QC}} \mathbf{\Lambda}_{NC} - \mathbf{W}_N^{\mathrm{T}} \mathbf{M}^{-1} \mathbf{W}_T \mathbf{\Lambda}_{T0C}^{(-)} + \dot{\mathbf{g}}_{NA} , \tag{30}$$

$$\dot{\mathbf{g}}_{TC} = \mathbf{W}_T^{\mathrm{T}} \mathbf{M}^{-1} \underbrace{(\mathbf{W}_N + \mathbf{W}_T \bar{\boldsymbol{\mu}}_S)}_{\mathbf{W}_{QC}} \mathbf{\Lambda}_{NC} - \mathbf{W}_T^{\mathrm{T}} \mathbf{M}^{-1} \mathbf{W}_T \mathbf{\Lambda}_{T0C}^{(-)} + \dot{\mathbf{g}}_{TA} . \tag{31}$$

Adding equations (26) and (27) gives the relation

$$\boldsymbol{\Lambda}_{T0C}^{(+)} = 2\bar{\bar{\boldsymbol{\mu}}}_S \boldsymbol{\Lambda}_{NC} - \boldsymbol{\Lambda}_{T0C}^{(-)}. \tag{32}$$

Equations (30), (31) and (32) set up an LCP on the velocity level for the compression phase

$$\begin{bmatrix} \dot{\mathbf{g}}_{NC} \\ \dot{\mathbf{g}}_{TC}^{-} \\ \boldsymbol{\Lambda}_{T0C}^{(+)} \end{bmatrix} = \begin{bmatrix} \mathbf{W}_N^{\mathrm{T}} \mathbf{M}^{-1} \mathbf{W}_Q & -\mathbf{W}_N^{\mathrm{T}} \mathbf{M}^{-1} \mathbf{W}_T & \mathbf{0}_{n_S \times n_S} \\ -\mathbf{W}_T^{\mathrm{T}} \mathbf{M}^{-1} \mathbf{W}_Q & \mathbf{W}_T^{\mathrm{T}} \mathbf{M}^{-1} \mathbf{W}_T & \mathbf{E}_{n_S \times n_S} \\ 2\bar{\bar{\boldsymbol{\mu}}}_S & -\mathbf{E}_{n_S \times n_S} & \mathbf{0}_{n_S \times n_S} \end{bmatrix} \begin{bmatrix} \boldsymbol{\Lambda}_{NC} \\ \boldsymbol{\Lambda}_{T0C}^{(-)} \\ \dot{\mathbf{g}}_{TC}^{+} \end{bmatrix} + \begin{bmatrix} \dot{\mathbf{g}}_{NA} \\ -\dot{\mathbf{g}}_{TA} \\ \mathbf{0}_{n_S \times 1} \end{bmatrix}. \tag{33}$$

where the decomposition (28) has been used.

3.3. Expansion Phase of Impact

In this subsection, we formulate an LCP for the expansion phase of the Poisson impact law, similar to the formulation of the compression phase. Again, all constraints that are elements of I_S are taken into account. The expansion phase is assumed to begin at a time t_C and to end at a time t_E, where the time difference $t_E - t_C$ is assumed to be "infinitely small". The equation of motion (19) is integrated over the expansion phase

$$\mathbf{M}(\dot{\mathbf{q}}_E - \dot{\mathbf{q}}_C) = [\mathbf{W}_N \quad \mathbf{W}_T] \begin{bmatrix} \boldsymbol{\lambda}_{NE} \\ \boldsymbol{\lambda}_{TE} \end{bmatrix}, \tag{34}$$

which yields the velocity jump over the expansion phase $\dot{\mathbf{q}}(t_E) - \dot{\mathbf{q}}(t_C) = \dot{\mathbf{q}}_E - \dot{\mathbf{q}}_C$ as a function of the impulses $\boldsymbol{\Lambda}_{NE}$ and $\boldsymbol{\Lambda}_{TE}$ in the normal and tangential directions defined by

$$\Lambda_{NEi} = \lim_{t_E \to t_C} \int_{t_C}^{t_E} \lambda_{Ni} \, \mathrm{d}t, \quad \Lambda_{TEi} = \lim_{t_E \to t_C} \int_{t_C}^{t_E} \lambda_{Ti} \, \mathrm{d}t, \quad i \in I_S. \tag{35}$$

At the end of expansion, each of the contact velocities must show non-negative values, $\dot{g}_{NEi} \geq 0$, because negative velocities would lead to further approach of the bodies and thus to penetration. The magnitudes of the contact velocities $\dot{g}_{NEi}$ depend on the strength of the expansion impulses. For coupled impact problems situations may occur where the original Poisson impulse $\varepsilon_{Ni} \Lambda_{NCi}$ in one of the contacts is not strong enough to prevent penetration because the contact partners are simultaneously under the influence of other impulsive forces. Thus, we generally have to allow impulses greater than the original Poisson impulse, $\Lambda_{NEi} \geq \varepsilon_{Ni} \Lambda_{NCi}$. If the Poisson impulse $\Lambda_{NEi} = \varepsilon_{Ni} \Lambda_{NCi}$ is strong enough to admit a separation, then any positive value of the contact velocity is allowed $\dot{g}_{NEi} \geq 0$. In the other case, the expansion impulse must be increased $\Lambda_{NEi} > \varepsilon_{Ni} \Lambda_{NCi}$ such that penetration is avoided, $\dot{g}_{NEi} = 0$. The impact law in the normal direction during expansion can now be stated by the complementarity condition

$$\Lambda_{NPi} \geq 0, \quad \dot{g}_{NEi} \geq 0, \quad \Lambda_{NPi}\, \dot{g}_{NEi} = 0; \quad i \in I_S, \tag{36}$$

with $\Lambda_{NPi} = \Lambda_{NEi} - \varepsilon_{Ni}\, \Lambda_{NCi}$. The tangential impact law for expansion is taken to be identical to compression:

$$\begin{aligned}
\dot{g}_{TEi} = 0 \quad &\Rightarrow \quad |\Lambda_{TEi}| \leq \mu_i \Lambda_{NEi} \quad \text{sticking} \\
\dot{g}_{TEi} < 0 \quad &\Rightarrow \quad \Lambda_{TEi} = +\mu_i \Lambda_{NEi} \quad \text{negative sliding} \quad i \in I_S. \\
\dot{g}_{TEi} > 0 \quad &\Rightarrow \quad \Lambda_{TEi} = -\mu_i \Lambda_{NEi} \quad \text{positive sliding}
\end{aligned} \tag{37}$$

A more advanced modeling (Glocker, 1995; Pfeiffer and Glocker 1996), which takes into account reversible portions of the tangential impulse (occurring in highly elastic materials such as superballs) is beyond the scope of this paper.

Evaluating the contact velocities (24) at t_C and t_E gives

$$\begin{bmatrix} \dot{\mathbf{g}}_{NE} \\ \dot{\mathbf{g}}_{TE} \end{bmatrix} = \begin{bmatrix} \mathbf{W}_N^{\mathrm{T}} \\ \mathbf{W}_T^{\mathrm{T}} \end{bmatrix} (\dot{\mathbf{q}}_E - \dot{\mathbf{q}}_C) + \begin{bmatrix} \dot{\mathbf{g}}_{NC} \\ \dot{\mathbf{g}}_{TC} \end{bmatrix} \quad \in \mathbb{R}^{2n_S}. \tag{38}$$

Completely analogous to the compression phase, we split the friction characteristic into two corners with the friction saturation impulses $\mathbf{\Lambda}_{T0E}^{(+)}$ and $\mathbf{\Lambda}_{T0E}^{(-)}$:

$$\mathbf{\Lambda}_{T0E}^{(+)} = \bar{\bar{\boldsymbol{\mu}}}_S\, \mathbf{\Lambda}_{NE} + \mathbf{\Lambda}_{TE} \tag{39}$$

$$\mathbf{\Lambda}_{T0E}^{(-)} = \bar{\bar{\boldsymbol{\mu}}}_S\, \mathbf{\Lambda}_{NE} - \mathbf{\Lambda}_{TE}. \tag{40}$$

We now express the friction saturations in terms of $\mathbf{\Lambda}_{NP}$

$$\mathbf{\Lambda}_{T0E}^{(+)} = \bar{\bar{\boldsymbol{\mu}}}_S\, \mathbf{\Lambda}_{NP} + \mathbf{\Lambda}_{TE} + \bar{\bar{\boldsymbol{\mu}}}_S\, \bar{\bar{\boldsymbol{\epsilon}}}_N\, \mathbf{\Lambda}_{NC} \tag{41}$$

$$\mathbf{\Lambda}_{T0E}^{(-)} = \bar{\bar{\boldsymbol{\mu}}}_S\, \mathbf{\Lambda}_{NP} - \mathbf{\Lambda}_{TE} + \bar{\bar{\boldsymbol{\mu}}}_S\, \bar{\bar{\boldsymbol{\epsilon}}}_N\, \mathbf{\Lambda}_{NC}. \tag{42}$$

Adding equations (41) and (42) gives the relation

$$\mathbf{\Lambda}_{T0E}^{(+)} = 2\bar{\bar{\boldsymbol{\mu}}}_S\, \mathbf{\Lambda}_{NP} - \mathbf{\Lambda}_{T0E}^{(-)} + 2\bar{\bar{\boldsymbol{\mu}}}_S\, \bar{\bar{\boldsymbol{\epsilon}}}_N\, \mathbf{\Lambda}_{NC}. \tag{43}$$

The velocity $\dot{\mathbf{g}}_{TE}$ is decomposed into

$$\dot{\mathbf{g}}_{TE} = \dot{\mathbf{g}}_{TE}^{+} - \dot{\mathbf{g}}_{TE}^{-}. \tag{44}$$

The impulse equation (20) together with equation (42) is substituted in the contact equations (38)

$$\dot{\mathbf{g}}_{NE} = \mathbf{W}_N^{\mathrm{T}}\mathbf{M}^{-1}\underbrace{(\mathbf{W}_N + \mathbf{W}_T\bar{\bar{\boldsymbol{\mu}}}_S)}_{\mathbf{W}_{QE}}\boldsymbol{\Lambda}_{NP} - \mathbf{W}_N^{\mathrm{T}}\mathbf{M}^{-1}\mathbf{W}_T\boldsymbol{\Lambda}_{T0E}^{(-)} + \underbrace{\mathbf{W}_N^{\mathrm{T}}\mathbf{M}^{-1}(\mathbf{W}_N + \mathbf{W}_T\bar{\bar{\boldsymbol{\mu}}}_S)\bar{\bar{\boldsymbol{\epsilon}}}_N\boldsymbol{\Lambda}_{NC}}_{\mathbf{b}_{NE}} + \dot{\mathbf{g}}_{NC} \tag{45}$$

$$\dot{\mathbf{g}}_{TE} = \mathbf{W}_T^{\mathrm{T}}\mathbf{M}^{-1}\underbrace{(\mathbf{W}_N + \mathbf{W}_T\bar{\bar{\boldsymbol{\mu}}}_S)}_{\mathbf{W}_{QE}}\boldsymbol{\Lambda}_{NP} - \mathbf{W}_T^{\mathrm{T}}\mathbf{M}^{-1}\mathbf{W}_T\boldsymbol{\Lambda}_{T0E}^{(-)} + \underbrace{\mathbf{W}_T^{\mathrm{T}}\mathbf{M}^{-1}(\mathbf{W}_N + \mathbf{W}_T\bar{\bar{\boldsymbol{\mu}}}_S)\bar{\bar{\boldsymbol{\epsilon}}}_N\boldsymbol{\Lambda}_{NC}}_{\mathbf{b}_{TE}} + \dot{\mathbf{g}}_{TC}\,. \tag{46}$$

Equations (45), (46) and (43) set up an LCP on the velocity level for the expansion phase

$$\begin{bmatrix} \dot{\mathbf{g}}_{NE} \\ \dot{\mathbf{g}}_{TE}^{-} \\ \boldsymbol{\lambda}_{T0E}^{(+)} \end{bmatrix} = \begin{bmatrix} \mathbf{W}_N^{\mathrm{T}}\mathbf{M}^{-1}\mathbf{W}_{QE} & -\mathbf{W}_N^{\mathrm{T}}\mathbf{M}^{-1}\mathbf{W}_T & \mathbf{0}_{n_S\times n_S} \\ -\mathbf{W}_H^{\mathrm{T}}\mathbf{M}^{-1}\mathbf{W}_{QE} & \mathbf{W}_T^{\mathrm{T}}\mathbf{M}^{-1}\mathbf{W}_T & \mathbf{E}_{n_S\times n_S} \\ 2\bar{\bar{\boldsymbol{\mu}}}_S & -\mathbf{E}_{n_S\times n_S} & \mathbf{0}_{n_S\times n_S} \end{bmatrix} \begin{bmatrix} \boldsymbol{\Lambda}_{NP} \\ \boldsymbol{\Lambda}_{T0E}^{(-)} \\ \dot{\mathbf{g}}_{TE}^{+} \end{bmatrix} + \begin{bmatrix} \mathbf{b}_{NE} + \dot{\mathbf{g}}_{NC} \\ -\mathbf{b}_{TE} - \dot{\mathbf{g}}_{TC} \\ 2\bar{\bar{\boldsymbol{\mu}}}_S\bar{\bar{\boldsymbol{\epsilon}}}_N\boldsymbol{\Lambda}_{NC} \end{bmatrix}. \tag{47}$$

where the decomposition (44) has been used.

3.4. The Integration Procedure

Figure 2 shows the order of the different phases in the integration procedure. The equation of motion for given index sets is numerically integrated until an impact, stick–slip or detachment event occurs. If the event is an impact event, then the LCPs for compression and expansion have to be solved, after which the new generalized velocities $\dot{\mathbf{q}}$ are known. Subsequently, an LCP on the acceleration level has to be solved, because the impact might cause stick–slip transitions or detachment of other contacts. The new accelerations $\ddot{\mathbf{q}}$ are known after having solved all necessary LCPs. The new index sets can then be set up and a new integration phase can start. Basically, any ODE solver can be used for the integration of the smooth phase as long as the solver supports event detection.

4. THE WOODPECKER TOY

The woodpecker toy is a toy with interesting dynamic behavior, showing both impact and friction phenomena (Figure 3). The toy consists of a sleeve, a spring and the woodpecker.

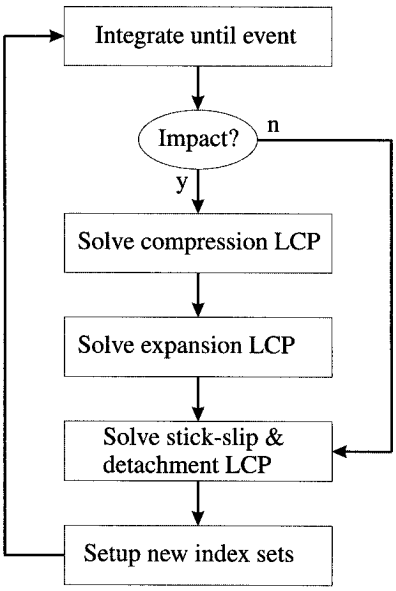

Figure 2. Flowchart of the algorithm.

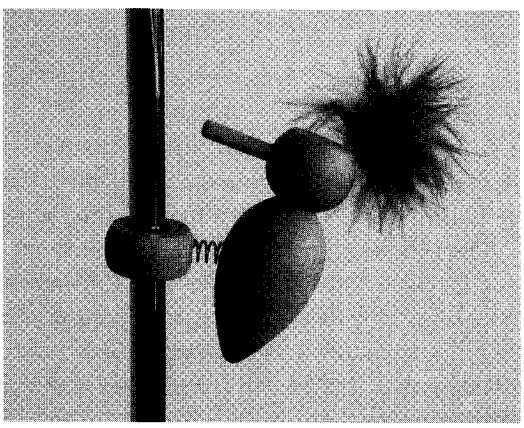

Figure 3. The woodpecker toy.

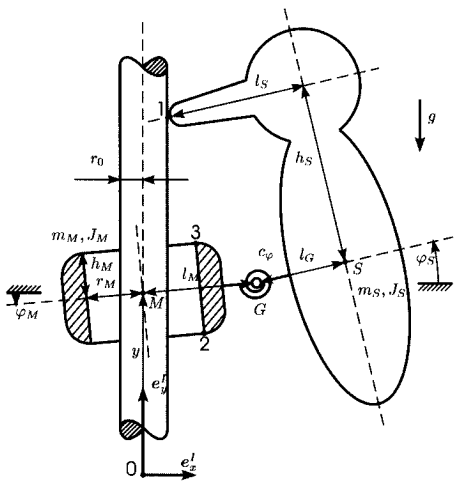

Figure 4. Model of the woodpecker toy (not to scale).

The hole in the sleeve is slightly larger than the diameter of the pole, thus allowing a kind of pitching motion interrupted by impacts with friction.

The scientific study of this toy dates back to Pfeiffer (1984). At that time, it was not possible to deal with systems with impact and friction. A heuristic model was presented in Pfeiffer (1984, 1991), in which the friction losses were determined experimentally. The lack of a more general theory stimulated the work of Glocker (1995) and Pfeiffer and Glocker (1996), who formulated the theory briefly presented in Section 3, which offers a sound basis for impact problems with friction. In Glocker (1995) and Pfeiffer and Glocker (1996), a model for the woodpecker toy was presented as example for the developed theory. In this section, we give a bifurcation analysis of the model presented in Glocker (1995) and Pfeiffer and Glocker (1996), with the aid of a one-dimensional mapping. First, the model is briefly given.

The woodpecker toy is a system that can only operate in the presence of friction as it relies on combined impacts and jamming. Restitution of the beak with the pole is not essential for a periodic motion but increases the resemblance with the typical behavior of a woodpecker. The motion of the toy lies in a plane, which reduces the number of degrees of freedom to model the system.

The system (Figure 4) possesses three degrees of freedom $\mathbf{q} = [y \quad \varphi_M \quad \varphi_S]^{\mathrm{T}}$, where φ_S and φ_M are the absolute angles of rotation of the woodpecker and the sleeve, respectively, and y describes the vertical displacement of the sleeve. Horizontal displacement of the sleeve is negligible. Due to the clearance between sleeve and pole, the lower or upper edge of the sleeve may come into contact with the pole, which is modeled by constraints 2 and 3. Furthermore, contact between the beak of the woodpecker with the pole is expressed by constraint 1. The special geometry of the design enables us to assume only small deviations of the rotations. Thus, a linearized evaluation of the system's kinematics is sufficient and leads to the model listed below. The mass matrix $\mathbf{M}$, the force vector $\mathbf{h}$ and the constraint vectors $\mathbf{w}$ follow from Figure 4 in a straightforward manner. They are

$$\mathbf{M} = \begin{bmatrix} (m_S + m_M) & m_S l_M & m_S l_G \\ m_S l_M & (J_S + m_S l_M^2) & m_S l_M l_G \\ m_S l_G & m_S l_M l_G & (J_S + m_S l_G^2) \end{bmatrix},$$

$$\mathbf{h} = \begin{bmatrix} -(m_S + m_M)g \\ -c_\varphi(\varphi_M - \varphi_S) - m_S g l_M \\ -c_\varphi(\varphi_S - \varphi_M) - m_S g l_G \end{bmatrix}$$

$$g_{N1} = (l_M + l_G - l_S - r_0) - h_S\varphi_S, \quad g_{N2} = (r_M - r_0) + h_M\varphi_M, \quad g_{N3} = (r_M - r_0) - h_M\varphi_M$$

$$\mathbf{w}_{N1} = \begin{bmatrix} 0 \\ 0 \\ -h_S \end{bmatrix}, \quad \mathbf{w}_{N2} = \begin{bmatrix} 0 \\ h_M \\ 0 \end{bmatrix}, \quad \mathbf{w}_{N3} = \begin{bmatrix} 0 \\ -h_M \\ 0 \end{bmatrix}$$

$$\mathbf{w}_{T1} = \begin{bmatrix} 1 \\ l_M \\ l_G - l_S \end{bmatrix}, \quad \mathbf{w}_{T2} = \begin{bmatrix} 1 \\ r_M \\ 0 \end{bmatrix}, \quad \mathbf{w}_{T3} = \begin{bmatrix} 1 \\ r_M \\ 0 \end{bmatrix} \tag{48}$$

$$\bar{\mathbf{w}}_N = \hat{\mathbf{w}}_N = \bar{\mathbf{w}}_T = \hat{\mathbf{w}}_T = \mathbf{0}.$$

4.1. Results

For the numerical analysis of the woodpecker toy, we consider the same data set as used in Glocker (1995) and Pfeiffer and Glocker (1996):

Dynamics $m_M = 0.0003$ kg, $J_M = 5.0 \times 10^{-9}$ kg m^2, $m_S = 0.0045$ kg, $J_S = 7.0 \times 10^{-7}$ kg m^2, $g = 9.81$ m/s^2;

Geometry $r_0 = 0.0025$ m, $r_M = 0.0031$ m, $h_M = 0.0058$ m, $l_M = 0.010$ m, $l_G = 0.015$ m, $h_S = 0.020$ m, $l_S = 0.0201$ m;

Contact $\mu_1 = \mu_2 = \mu_3 = 0.3$, $\varepsilon_{N1} = 0.5$, $\varepsilon_{N2} = \varepsilon_{N3} = 0.0$.

The motions of the sleeve and the woodpecker are limited by the contacts, $|\varphi_M| \leq (r_M - r_0)/h_M = 0.1034$ rad and $\varphi_S \leq (l_M + l_G - l_S - r_0)/h_S = 0.12$ rad. The system has a (marginally stable) equilibrium position, in which the woodpecker is hanging backward on the jamming sleeve, $\mathbf{q} = [y \quad -0.1034 \quad -0.2216]^{\mathrm{T}}$. The jamming of the sleeve with the pole at that position is only possible if $\mu_2 \geq 0.285$. The equilibrium point is marginally stable because no damping is modeled between the woodpecker and the sleeve, but is stable in practice due to ever existing dissipation in reality.

Using the above data set, the motion of the woodpecker was simulated and a stable periodic solution was found with period $T = 0.1452$ s. The time history of two periods

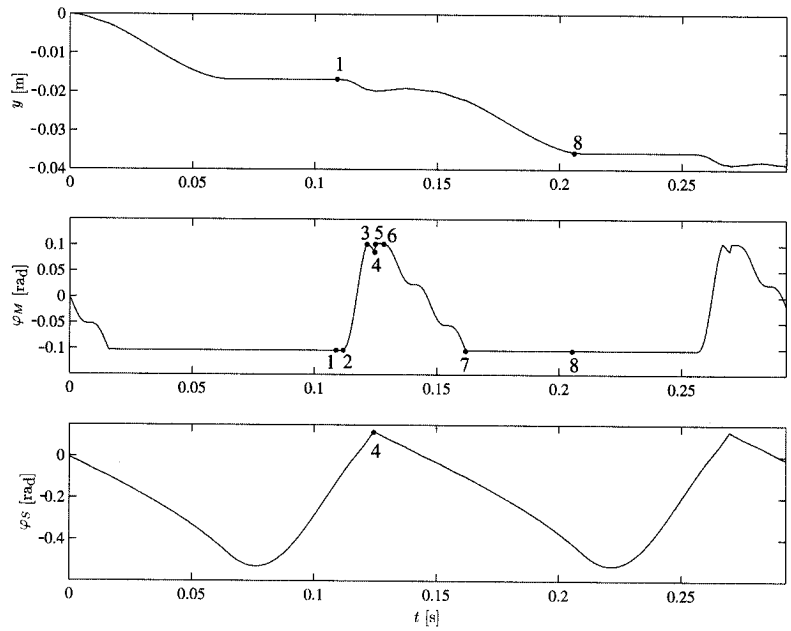

Figure 5. Time history of the coordinates.

of this periodic solution are shown in Figure 5 and the corresponding phase space portraits in Figure 6. The numbers 1–8 correspond with the frames depicted in Figure 7. Let t_k denote the time at frame k. Just before $t = t_1$, the sleeve jams and the woodpecker rotates upward, thereby reducing the normal force in contact 2. At $t = t_1$, the sleeve starts sliding downward, due to the reduced normal contact force, and contact is lost at $t = t_2$. In the time interval $t_2 < t < t_3$, the toy is in free fall and quickly gains kinetic energy. The first upper sleeve impact occurs at $t = t_3$ but the contact immediately detaches. A beak impact occurs at $t = t_4$, which changes the direction of motion of the woodpecker. The beak impact is soon followed by the second upper sleeve impact at $t = t_5$. Detachment of the upper sleeve contact occurs at $t = t_6$. The toy is again in unconstrained motion during the time interval $t_6 < t < t_7$. A high-frequency oscillation can be observed during this time interval corresponding to the 72.91 Hz eigenfrequency of the woodpecker–spring–sleeve combination. Impact of the lower sleeve occurs at $t = t_7$, after which the sleeve slides down. The woodpecker rotates downward, increasing the normal force, and jamming of the sleeve starts at $t = t_8$. The succession of sliding and jamming of contact 2 transfers the kinetic energy of the translational motion in the y-direction, obtained during free fall, into rotational motion of the woodpecker. The woodpecker therefore swings backward when the lower sleeve contact jams, stores potential energy in the spring and swings forward again, $t = t_1 + T$, which completes the periodic motion.

Note that due to the completely filled mass matrix $\mathbf{M}$, an impact in one of the constraints affects each of the coordinates, which can be seen by the velocity jumps in the time histories and phase portraits of Figures 5 and 6.

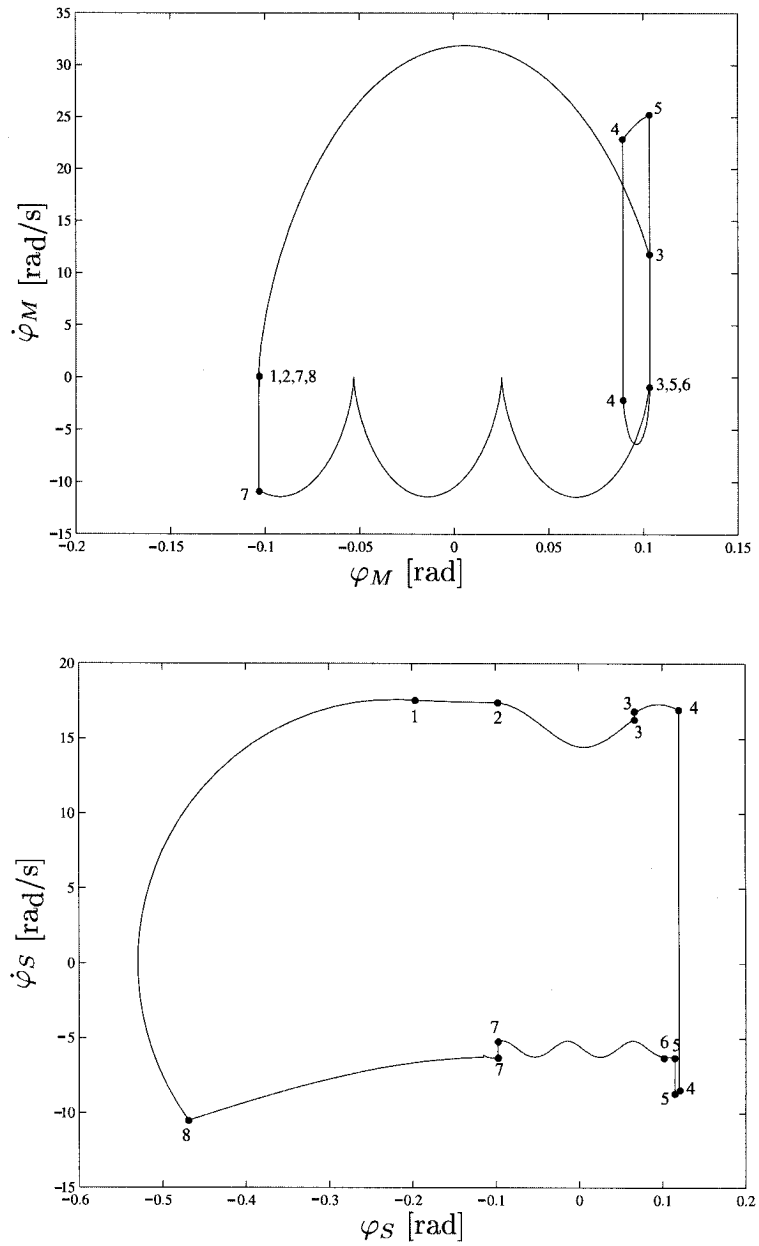

Figure 6. Phase space portraits.

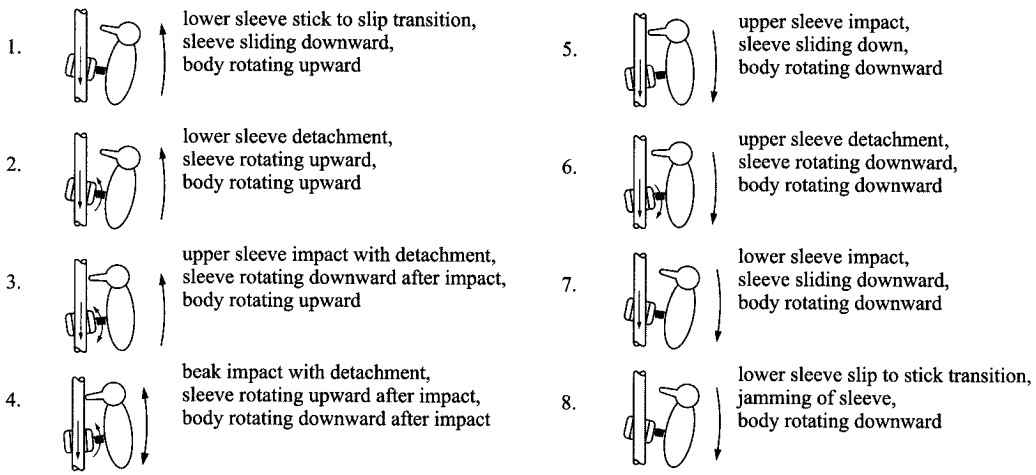

Figure 7. Sequence of events of the woodpecker toy (arrows indicate motion after impact).

The system has three degrees of freedom, which sets up a six-dimensional state space $(\mathbf{q}, \dot{\mathbf{q}}) \in \mathbb{R}^6$. However, the accelerations $\ddot{\mathbf{q}}$ are only dependent on $\mathbf{z} = (\varphi_M, \varphi_S, \dot{\mathbf{q}}) \in \mathbb{R}^5$ and not on the vertical displacement y. The six-dimensional system can therefore be looked upon as a set of a five-dimensional reduced system $\dot{\mathbf{z}} = \mathbf{f}(\mathbf{z})$ and a one-dimensional differential equation $\dot{y} = g(\mathbf{z})$. The on-average decreasing displacement y can never be periodic. By a periodic solution of the system, we mean periodic motion of the five states $\mathbf{z}$.

The reduced system $\mathbf{f}(\mathbf{z})$ possesses a set of solutions

$$\varphi_M = \varphi_S, |\varphi_M| \leq (r_M - r_0)/h_M = 0.1034, \dot{\varphi}_M = \dot{\varphi}_S = \mathbf{0},$$

which correspond to a free-falling motion of the toy along the shaft. This free fall can indeed be observed in the real toy, abruptly ended by the basement on which the shaft is mounted.

During the interval $t_8 < t < t_1 + T$, the sleeve jams and the woodpecker achieves a minimum rotation of $\varphi_S = -0.53$ rad. The rotation φ_S is the only non-constrained degree of freedom during jamming, which allows for a one-dimensional Poincaré mapping. Consider the one-dimensional hyperplane Σ as a section of the five-dimensional reduced phase space defined by

$$\Sigma = \{(\varphi_M, \varphi_S, \dot{\mathbf{q}}) \in \mathbb{R}^5 \mid \varphi_M = -(r_M - r_0)/h_M, \dot{\mathbf{q}} = \mathbf{0}\}. \tag{49}$$

If the woodpecker arrives at a local extremum during jamming, then the state $\mathbf{z}$ must lie on Σ. From a state $\mathbf{z}_k \in \Sigma$, a solution evolves which may return to Σ at $\varphi_S = \varphi_{S_{k+1}}$. We define the one-dimensional first return map $P : \Sigma \to \Sigma$ as

$$\varphi_{S_{k+1}} = P(\varphi_{S_k}). \tag{50}$$

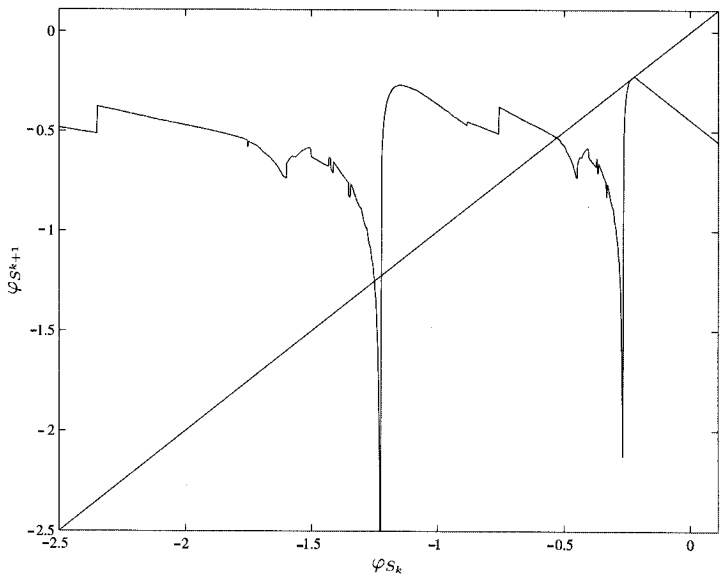

Figure 8. Poincaré map, $\varepsilon_{N1} = 0.5$.

Periodic solutions and equilibria, which achieve a local extremum during jamming of the sleeve, are fixed points of P. Periodic solutions might exist, at least in theory, which do not contain a jamming part during the period (for instance when the friction coefficient μ_2 is small). Those types of solutions cannot be found by using this Poincaré map. Still, the map P is suitable to study the manufacturers' intended operation of the toy, which is a period-1 solution with jamming, and deviations from this periodic motion.

The Poincaré map P for $\varepsilon_{N1} = 0.5$ is shown in Figure 8, obtained by numerical integration with 1000 initial values of φ_{S_k} (uniformly distributed between $-2.5 < \varphi_S < 0.11$). The map appears to be very irregular and shows two distinct dips at $\varphi_S = -1.23$ and $\varphi_S = -0.27$. These initial conditions lead to solutions evolving to the free-falling motions along the shaft, and will consequently never return to the hyperplane Σ. Initial conditions around these singularities lead to solutions which fall for some time along the shaft, but finally return to constrained motion and to the section Σ. The kinetic energy, built up during the free fall, causes the woodpecker to swing tremendously backward, which explains the form of the dip; the smaller the return value $\varphi_{S_{k+1}}$, the longer the fall time. The map has no value at the center of the dip, because the solution does not return to the Poincaré section. The dips are infinitely deep, but become smaller and steeper near the center. A finite depth is depicted due to the finite numerical accuracy. The rightmost dip consists of solutions which are directly trapped by the falling motion, whereas the left dip consists of solutions which first have an upper-sleeve impact before being trapped. More dips exist left of the depicted domain, all characterized by a sequence of events before the solution comes into free fall.

Several points can be observed in Figure 8, on which the map is discontinuous (for instance at $\varphi_{S_k} = -0.76$ and -2.35). The solution from an initial condition on the section Σ undergoes a sequence of events (impacts, stick–slip transitions) before returning to Σ. The

order, type and number of events in the sequence change for varying initial conditions φ_{S_k}. When the order of two events changes at a critical initial condition φ_{S_c}, then a discontinuity in the solution occurs with respect to the initial condition; see Brogliato (1999) and references therein. This discontinuity with respect to initial condition causes discontinuities in the Poincaré map. At the values $\varphi_{S_k} = -0.76$ and -2.35 for instance, the order of an upper sleeve impact and a beak impact are interchanged.

The Poincaré map P has been calculated for 94 different values (not uniformly distributed) of the beak restitution coefficient ε_{N1} (where each mapping takes about one hour of computation time). A bifurcation diagram was constructed from the set of mappings P by finding the crossings of the maps with the diagonal $\varphi_{S_{k+1}} = \varphi_{S_k}$. Each crossing is, for a locally smooth mapping, a stable or unstable periodic solution or equilibrium. The stability depends on the slope of the mapping at the crossing with the diagonal. The map P is discontinuous and also the jumps in the map can have crossings with the diagonal. Those discontinuous crossings are, however, not periodic solutions or equilibria.

Figure 9 shows the period-1 solutions of the woodpecker toy for varying ε_{N1}. Black lines indicate stable periodic solutions, and light gray lines denote unstable periodic solutions. The woodpecker can oscillate with small amplitude around the equilibrium point. These solutions are centers, due to the lack of damping between the sleeve and the woodpecker, and are indicated by a dark gray band in Figure 9 around the equilibrium at $\varphi_S = -0.2216$. Discontinuous crossings of the map with the diagonal are indicated by dotted lines and connect stable and unstable branches of periodic solutions. There exists a critical initial condition on the Poincaré section for which the solution after some time has two impact events that occur simultaneously: the beak impact and the upper sleeve impact. The order of the impacts changes when the initial condition is changed around this critical initial condition. This gives a discontinuity in the Poincaré map at the fixed value of the critical initial condition. The return values before and after the jump are, however, dependent on the restitution coefficient. The jump crosses the diagonal for some ranges of the restitution coefficient. These branches of discontinuity crossings are, of course, straight horizontal lines in Figure 9 because the critical initial condition is not dependent on the restitution coefficient.

Two stretched islands, I_1 and I_2, with unstable periodic solutions and discontinuous crossings can be observed in Figure 9. They are created by the two dips in the Poincaré map (Figure 8). It should be noted that the bifurcation diagram in Figure 9 is not complete. Small islands and additional branches of periodic solutions/discontinuous crossings might have been lost by the finite accuracy and the finite domain of the P map. More islands probably exist due to additional dips left of the considered domain.

From the P maps we can, in theory, construct higher-order maps P_j, $j = 2, 3, \ldots$ by mapping P onto itself, but the accuracy of the maps decreases for increasing order due to the finite discretization of P. The set of P_2 maps was constructed from the set of maps P. Figure 10 shows the period-2 solutions/discontinuous crossings (and also the period-1 solutions/crossings), obtained by finding the crossings of P_2 with the diagonal. Many additional branches appear in Figure 10, some branches of period-2 solutions, others discontinuous crossings of P_2 with the diagonal. Higher-order branches (three and higher) most surely also exist, but could not be computed accurately from P.

Branches of period-2 solutions appear in Figure 10 in pairs, as can be expected. It must hold for a period-2 solution that $\varphi_{S_{k+2}} = \varphi_{S_k}$ and $\varphi_{S_{k+3}} = \varphi_{S_{k+1}}$. In general, it holds that $\varphi_{S_{k+1}}$ is not equal to φ_{S_k} and they therefore appear as two different crossings in the P_2

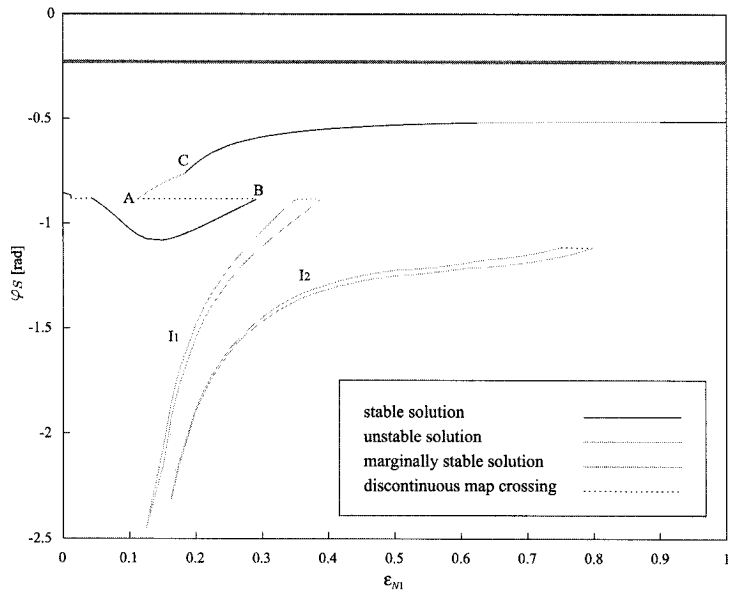

Figure 9. Bifurcation diagram, period-1 solutions.

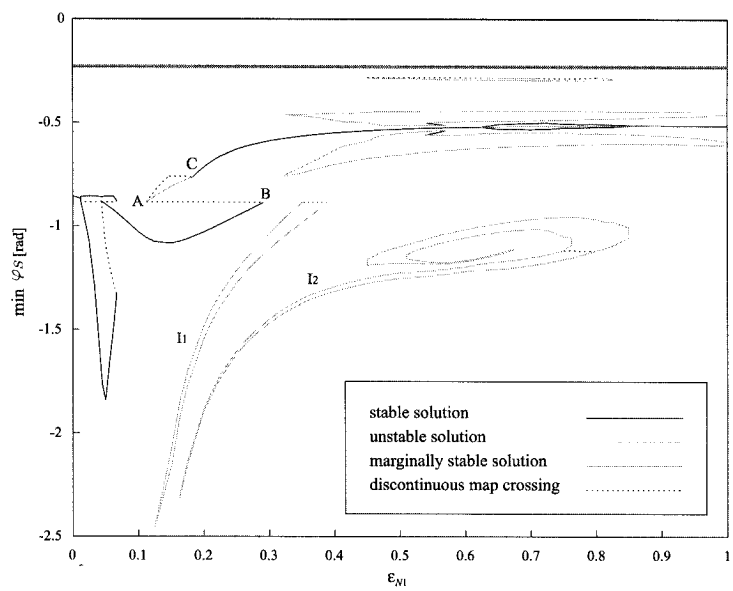

Figure 10. Bifurcation diagram, period-1 and period-2 solutions.

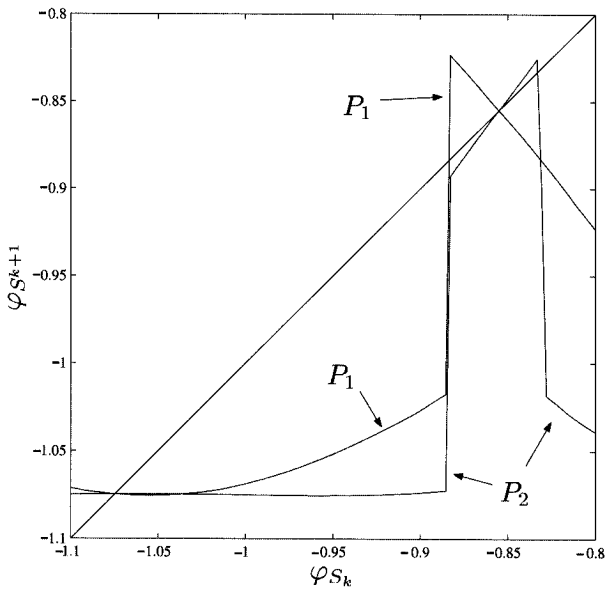

Figure 11. Zoom of the Poincaré maps for $\varepsilon_{N1} = 0.125$.

map and as different branches in the bifurcation diagram. The two branches of one pair just contain the same periodic solution but shifted in time.

It is very remarkable that the discontinuity crossings of P_2 do not appear in pairs, as can be seen for example at point A in Figure 10. At point A the branch of unstable period-1 solutions turns around and becomes a branch of P_1 discontinuity crossings, after which it is folded back to a stable branch at point B. A branch of P_2 discontinuity crossings bifurcates from the period-1 branch at A and makes a connection with point C. The P_2 discontinuity branch between A and C is clearly single (not a pair). More insight into what exactly happens at the non-conventional bifurcation point A can be gained from a local analysis of the mappings P and P_2. Figure 11 shows a zoom of P and P_2 around the crossings of interest for $\varepsilon_{N1} = 0.125$, which is between A and C. The map P is locally discontinuous and crosses the diagonal three times, leading to a stable and unstable solution and a discontinuity crossing. Studying the movement of the map for changing ε_{N1}, the map appeared to shift upward for increasing ε_{N1}. We now study a simple piecewise linear discontinuous map, which locally approximates the numerically obtained P-map.

Consider the piecewise linear mapping, dependent on the constants $a > 1$ and r,

$$P^L(x) = \begin{cases} -2 + r, & x \leq 0 \\ -ax + r, & x > 0 \end{cases} \tag{51}$$

which is depicted on the left in Figure 12 for $a = \frac{5}{4}$ and $r = 1$. The map shifts upward for increasing values of r. The map has two regular crossings with the diagonal

$$x = \frac{r}{1+a} > 0, \quad x = -2 + r < 0$$

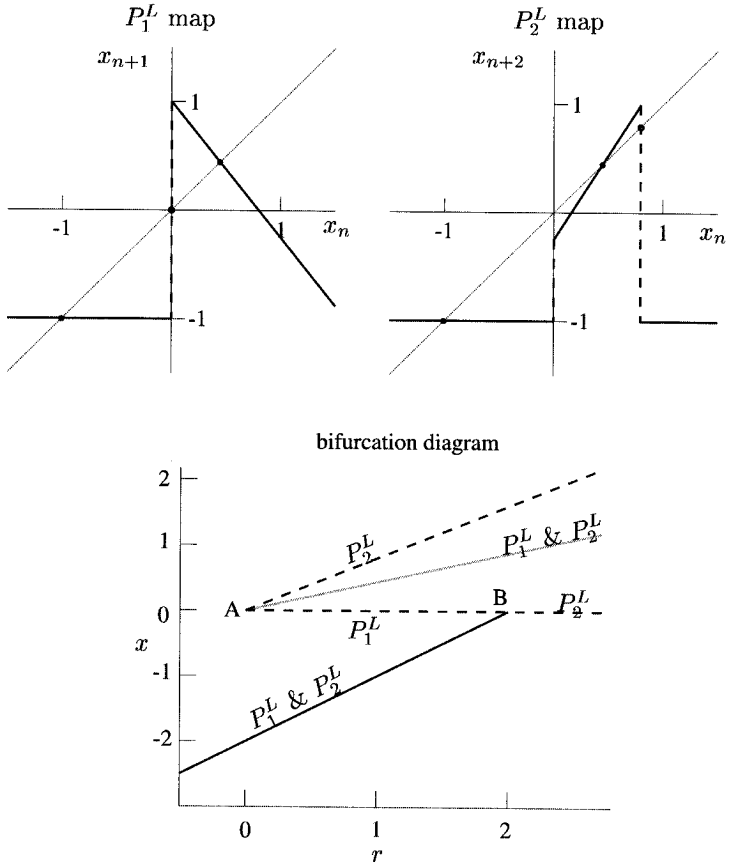

Figure 12. Analytical analysis of point A in Figure 10.

for $r > 0$ and $r < 2$, respectively. A discontinuous crossing exists at $x = 0$ for $0 < r < 2$. Mapping $P^L(x)$ onto itself gives $P_2^L(x)$

$$P_2^L(x) = \begin{cases} -2 + r, & x \leq 0 \\ a^2 x + (1-a)r, & 0 < x < \frac{r}{a} \\ -2 + r, & x \geq 0 \end{cases} \tag{52}$$

and is depicted in the right picture of Figure 12. The $P_2^L(x)$ map is again piecewise linear in x and has two discontinuities at $x = 0$ and $x = \frac{r}{a}$. The same regular crossings of P^L appear, of course, in P_2^L. Additionally, $P_2^L(x)$ has a *single* discontinuous crossing with the diagonal at $x = \frac{r}{a}$ but does not contain a discontinuous crossing at $x = 0$, like P^L. Note that P^L and P_2^L look indeed similar to P and P_2 in Figure 11. Varying r gives the bifurcation diagram depicted on the right of Figure 12, which is similar to what can be observed in Figure 10 around point A. Point B is also retrieved from the piecewise linear analysis. The local analysis by the piecewise linear map only predicts the behavior in a small neighbourhood of point A.

The bifurcation at point C is due to other changes in the map P and can therefore not be observed in Figure 12.

Note that regular crossings of P^L are also regular crossings of P_2^L, because they correspond to the periodic solutions and equilibria of the system. Discontinuous crossings of P^L are in general *not* necessarily discontinuous crossings of P_2^L.

Branches of higher-order discontinuous crossings of P_j^L and $j > 2$ also start at point A. It can therefore be expected that these branches can also be found for the woodpecker toy if the higher-order maps are calculated accurately.

Bifurcation point A shows behavior similar to a fold bifurcation, at which a branch is folded around, albeit that the branch changes to a branch of discontinuous crossings after folding. Apart from the folding action, also a branch with P_2 discontinuous crossings bifurcates from the period-1 branch at point A. In some sense, this behavior is similar to a flip or period-doubling bifurcation, at which a period-doubled solution bifurcates from the period-1 branch. The bifurcation point A therefore shows both folding and a kind of flip action. This does not conform with the bifurcation theory for smooth systems, which predicts that bifurcations are either fold or flip bifurcations (or of other type). Bifurcation point A is therefore a non-conventional bifurcation point. A similar bifurcation point, showing both fold and flip action, was found for a Filippov type of system in Leine et al. (2000) and Leine (2000). The combined fold–flip behavior is related to the tent map, which is more elaborately explained in Leine et al. (2000) and Leine (2000). Note that the P map shows indeed a peak, similar to the tent map, although one flange is vertical.

The nonlinear dynamics of the woodpecker toy has been studied in this section. The analysis is not complete, because many other parameters can be varied. The chaotic attractors have also not been considered. Still, the variation of ε_{N1} gives more insight into the complex dynamical phenomena present in the system. A one-dimensional mapping was found for the woodpecker toy. This mapping turns out to be very valuable for the construction of bifurcation diagrams, because it detects not only the periodic solutions but also the discontinuity crossings. Branches of discontinuity crossings appear to connect branches of periodic solutions and are therefore a new type of object in the bifurcation diagram, different from attractors. Furthermore, the one-dimensional mapping can be used to gain a better understanding of non-conventional bifurcation points.

5. THE TUMBLING TOY

In this section we study the nonlinear dynamics of the tumbling toy (Figure 13) using the rigid multibody theory of Section 3. The toy consists of a hollow wooden body with two pivots on each side (Figure 14). Within the body is a metal ball, which can roll free along the main axis of the body. The body can tumble down an inclined saw-toothed wooden rail, on which the pivots step down the teeth of the rail. The tumbling motion is characterized by the alternating rotation of the body around one of the two pivots with the rolling of the ball from one side of the body to the other. The system possesses four degrees of freedom $\mathbf{q} = [y_S \quad \varphi_S \quad x_B \quad x_S]^{\mathrm{T}}$. The coordinates x_S and y_S describe the tangential and normal displacement of the center of mass of the body with respect to the rail, and φ_S is the rotation with respect to the rail. The coordinate x_B is the displacement of the ball within the body. The maximum displacement of the ball is $x_B = \pm l$. The motion of the tumbling toy is governed

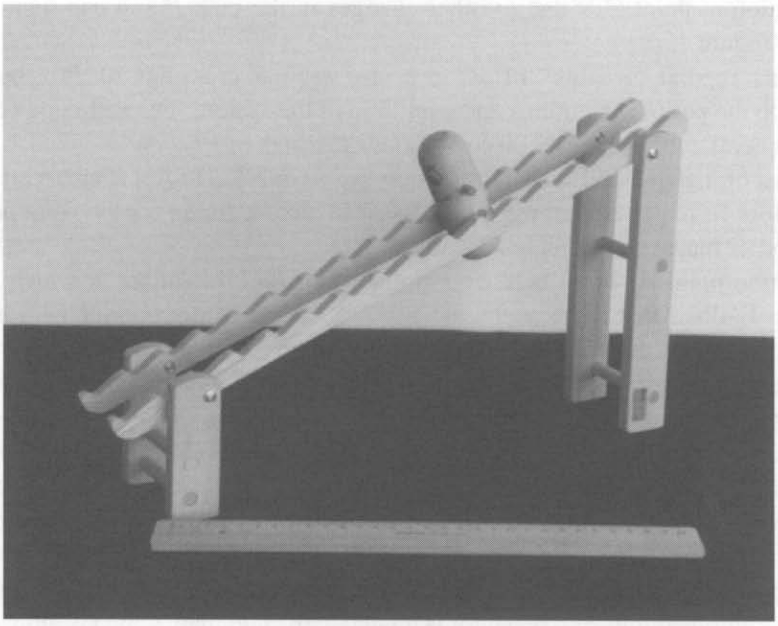

Figure 13. The tumbling toy.

by impacts. Friction forces between the pivots and rail are small and will be neglected. The ball in the body will be considered as a point mass moving without friction within the body. The mass matrix $\mathbf{M}$ and force vector $\mathbf{h}$ can be derived in a straightforward manner. They are

$$\mathbf{M} = \begin{bmatrix} (m_S + m_B) & 0 & -m_B x_B \sin\varphi_S & m_B \cos\varphi_S \\ 0 & (m_S + m_B) & m_B x_B \cos\varphi_S & m_B \sin\varphi_S \\ -m_B x_B \sin\varphi_S & m_B x_B \cos\varphi_S & (J_S + m_B x_B^2) & 0 \\ m_B \cos\varphi_S & m_B \sin\varphi_S & 0 & m_B \end{bmatrix} \tag{53}$$

$$\mathbf{h} = \begin{bmatrix} -(m_S + m_B) g \sin\varphi_R + 2m_B \dot{x}_B \dot{\varphi}_S \sin\varphi_S + m_B x_B \dot{\varphi}_S^2 \cos\varphi_S \\ -(m_S + m_B) g \cos\varphi_R - 2m_B \dot{x}_B \dot{\varphi}_S \cos\varphi_S + m_B x_B \dot{\varphi}_S^2 \sin\varphi_S \\ -m_B g x_B \cos(\varphi_S + \varphi_R) - 2m_B x_B \dot{x}_B \dot{\varphi}_S \\ -m_B g \sin(\varphi_S + \varphi_R) + m_B x_B \dot{\varphi}_S^2 \end{bmatrix} \tag{54}$$

The contact distances $\mathbf{g}_N$ and constraint vectors $\mathbf{w}$ for the contact between the ball and the body (contact points 1 and 2 in Figure 14) are also straightforward and are given by

$$g_{N1} = l - x_B, \quad g_{N2} = l + x_B, \tag{55}$$

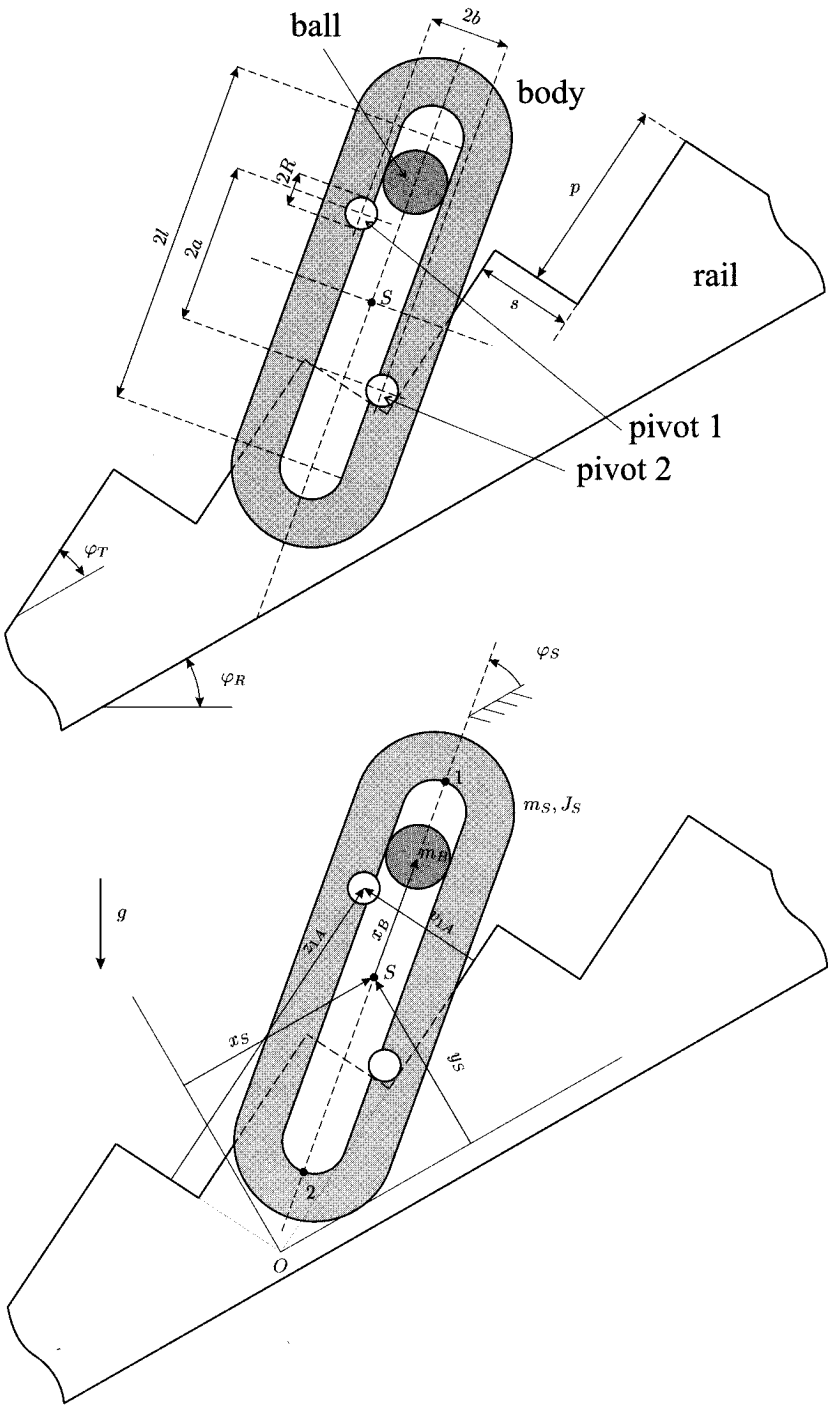

Figure 14. Model of the tumbling toy: top, geometry; bottom, coordinates.

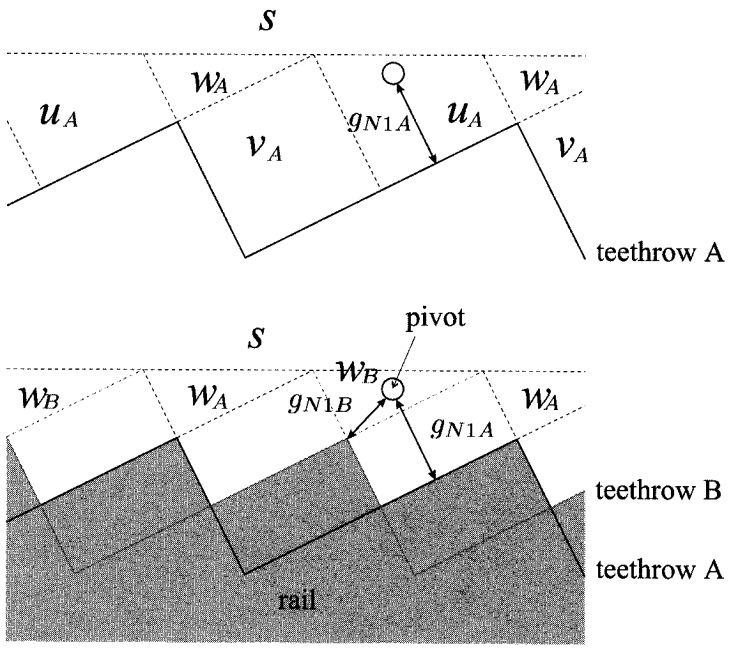

Figure 15. Teeth contact spaces.

$$\mathbf{w}_{N1} = [0 \quad 0 \quad 0 \quad -1]^{\mathrm{T}}, \quad \mathbf{w}_{N2} = [0 \quad 0 \quad 0 \quad 1]^{\mathrm{T}}. \tag{56}$$

Formulation of the contact distances $\mathbf{g}_N$ and constraint vectors $\mathbf{w}$ for the pivot–rail contacts is more cumbersome due to the saw-tooth profile of the rail. The saw-toothed rail can be in double-point contact with a pivot (like the lower pivot in Figure 14). Such a corner point can be envisaged as the intersection of two simple unilateral smooth constraints. We therefore describe the rail by two double-pitched teeth-rows, A and B, being in anti-phase with each other (see Figure 15). If a pivot is in double-point contact with the rail, then it is in single-point contact with both teeth-rows A and B, which circumvents the problem.

We introduce the constants d_x and d_y and functions D_1 and D_2 of φ_S, which will be used in the following:

$$d_x = a\cos\varphi_T + b\sin\varphi_T, \quad d_y = a\sin\varphi_T - b\cos\varphi_T, \tag{57}$$

$$D_1 = d_x\cos\varphi_S + d_y\sin\varphi_S, \quad D_2 = d_y\cos\varphi_S - d_x\sin\varphi_S. \tag{58}$$

Differentiation of the latter functions gives $\dot{D}_1 = D_2\dot{\varphi}_S$ and $\dot{D}_2 = -D_1\dot{\varphi}_S$.

We now define coordinates z_{ij} and v_{ij}, $i = 1, 2$ and $j = \mathrm{A}, \mathrm{B}$, of the centers of pivots 1 and 2 along the flanges of teeth-rows A and B (see Figure 14). These are

$$
\begin{aligned}
z_{1A} &= x_S \cos\varphi_T + y_S \sin\varphi_T + D_1, \quad z_{1B} = z_{1A} - p \\
z_{2A} &= x_S \cos\varphi_T + y_S \sin\varphi_T - D_1, \quad z_{2B} = z_{2B} - p
\end{aligned} \tag{59}
$$

$$
\begin{aligned}
v_{1A} &= -x_S \sin\varphi_T + y_S \cos\varphi_T - D_2, \quad v_{1B} = v_{1A} + s \\
v_{2A} &= -x_S \sin\varphi_T + y_S \cos\varphi_T + D_2, \quad v_{2B} = v_{2A} + s
\end{aligned} \tag{60}
$$

A second problem forms the multitude of the teeth. As we do not want to take all teeth into the description at the same time instant, we have to define modulated coordinates $\tilde{z}_{ij}$ and $\tilde{v}_{ij}$

$$
\tilde{z}_{ij} = z_{ij} \mod 2p, \qquad \tilde{v}_{ij} = v_{ij} \mod 2s. \tag{61}
$$

The heights h_1 and h_2 of pivots 1 and 2 with respect to the x_S-axis are

$$
\begin{aligned}
h_1 &= z_{1A} \sin\varphi_T + v_{1A} \cos\varphi_T - R = y_S + a\sin\varphi_S + b\cos\varphi_S \\
h_2 &= z_{2A} \sin\varphi_T + v_{2A} \cos\varphi_T - R = y_S - a\sin\varphi_S - b\cos\varphi_S
\end{aligned} \tag{62}
$$

We are now able to define the following spaces in which a pivot can be located (see Figure 15) with the modulated coordinates and pivot heights:

$$
\begin{aligned}
\mathcal{U}_{ij} &= \{(\tilde{z}_{ij}, \tilde{v}_{ij}) \in \mathbb{R}^2 \mid h_i < h_c \wedge \tilde{z}_{ij} > p\}, \\
\mathcal{V}_{ij} &= \{(\tilde{z}_{ij}, \tilde{v}_{ij}) \in \mathbb{R}^2 \mid h_i < h_c \wedge \tilde{z}_{ij} \leq p \wedge \tilde{v}_{ij} > s\}, \\
\mathcal{W}_{ij} &= \{(\tilde{z}_{ij}, \tilde{v}_{ij}) \in \mathbb{R}^2 \mid h_i < h_c \wedge \tilde{z}_{ij} \leq p \wedge \tilde{v}_{ij} \leq s\}, \\
\mathcal{S}_i &= \{(\tilde{z}_{ij}, \tilde{v}_{ij}) \in \mathbb{R}^2 \mid h_i \geq h_c\}.
\end{aligned} \tag{63}
$$

Each tooth is surrounded by the three spaces $\mathcal{U}_{ij}$, $\mathcal{V}_{ij}$ and $\mathcal{W}_{ij}$. The space $\mathcal{S}_i$ defines a region where the pivot is 'far' away from the teeth-row. The contact distances g_{Nij} of the pivots to teeth-rows A and B can now be expressed for each space:

$$
g_{Nij} = \begin{cases}
\tilde{v}_{ij} - R & (\tilde{z}_{ij}, \tilde{v}_{ij}) \in \mathcal{U}_{ij} \\
\tilde{z}_{ij} - R & (\tilde{z}_{ij}, \tilde{v}_{ij}) \in \mathcal{V}_{ij} \\
\sqrt{\tilde{z}_{ij}^2 + \tilde{v}_{ij}^2} - R & (\tilde{z}_{ij}, \tilde{v}_{ij}) \in \mathcal{W}_{ij} \\
\infty & (\tilde{z}_{ij}, \tilde{v}_{ij}) \in \mathcal{S}_i.
\end{cases} \tag{64}
$$

The contact distance in space $\mathcal{S}_i$ is set to ∞, but we can take any positive value. If the pivot is located in one of the three other spaces, then contact might occur. The contact distance

stands normal to the closest flange and to the pivot within spaces $\mathcal{U}_{ij}$ and $\mathcal{V}_{ij}$. Within the space $\mathcal{W}_{ij}$ is the upper corner of the tooth, the closest point to the pivot. The contact vectors $\mathbf{w}_{Nij}$ and $\bar{\mathbf{w}}_{Nij}$, which only need to be known when the contact is closed, become

$$\mathbf{w}_{Nij} = \begin{cases} \mathbf{u}_{vi} & (\tilde{z}_{ij}, \tilde{v}_{ij}) \in \mathcal{U}_{ij} \\ \mathbf{u}_{zi} & (\tilde{z}_{ij}, \tilde{v}_{ij}) \in \mathcal{N}_{ij} \\ (\tilde{z}_{ij}\, \mathbf{u}_{zi} + \tilde{v}_{ij}\, \mathbf{u}_{vi})/r_{ij} & (\tilde{z}_{ij}, \tilde{v}_{ij}) \in \mathcal{W}_{ij} \end{cases} \tag{65}$$

$$\bar{w}_{N1j} = \begin{cases} D_2\dot{\varphi}_S^2 & (\tilde{z}_{1j}, \tilde{v}_{1j}) \in \mathcal{U}_{1j} \\ -D_1\dot{\varphi}_S^2 & (\tilde{z}_{1j}, \tilde{v}_{1j}) \in \mathcal{V}_{1j} \\ \frac{(\tilde{v}_{1j}\, D_2 - \tilde{z}_{1j}\, D_1)\dot{\varphi}_S^2 + \dot{z}_{1j}^2 + \dot{v}_{1j}^2}{r_{1j}} - \frac{\tilde{z}_{1j}\, \dot{z}_{1j} + \tilde{v}_{1j}\, \dot{v}_{1j}}{r_{1j}^3} & (\tilde{z}_{1j}, \tilde{v}_{1j}) \in \mathcal{W}_{1j} \end{cases} \tag{66}$$

$$\bar{w}_{N2j} = \begin{cases} -D_2\dot{\varphi}_S^2 & (\tilde{z}_{2j}, \tilde{v}_{2j}) \in \mathcal{U}_{2j} \\ D_1\dot{\varphi}_S^2 & (\tilde{z}_{2j}, \tilde{v}_{2j}) \in \mathcal{V}_{2j} \\ \frac{(-\tilde{v}_{2j}\, D_2 + \tilde{z}_{2j}\, D_1)\dot{\varphi}_S^2 + \dot{z}_{2j}^2 + \dot{v}_{2j}^2}{r_{2j}} - \frac{\tilde{z}_{2j}\, \dot{z}_{2j} + \tilde{v}_{2j}\, \dot{v}_{2j}}{r_{2j}^3} & (\tilde{z}_{2j}, \tilde{v}_{2j}) \in \mathcal{W}_{2j} \end{cases} \tag{67}$$

where $r_{ij} = \sqrt{\tilde{z}_{ij}^2 + \tilde{v}_{ij}^2}$ and

$$\begin{aligned} \mathbf{u}_{z1} &= [\cos\varphi_T \quad \sin\varphi_T \quad D_2 \quad 0]^{\mathrm{T}} \qquad \mathbf{u}_{v1} = [-\sin\varphi_T \quad \cos\varphi_T \quad D_1 \quad 0]^{\mathrm{T}} \\ \mathbf{u}_{z2} &= [\cos\varphi_T \quad \sin\varphi_T \quad -D_2 \quad 0]^{\mathrm{T}} \quad \mathbf{u}_{v2} = [-\sin\varphi_T \quad \cos\varphi_T \quad -D_1 \quad 0]^{\mathrm{T}} \end{aligned}, \tag{68}$$

$$\dot{z}_{ij} = u_{zi}^T \dot{q}, \quad \dot{v}_{ij} = u_{vi}^T \dot{q}. \tag{69}$$

The contact distances and contact vectors of ball–body contact and pivot–rail contact are gathered in the vector $\mathbf{g}_N$, matrix $\mathbf{W}_N$ and vectors $\bar{\mathbf{w}}_N$, $\hat{\mathbf{w}}_N$ as

$$\mathbf{g}_N = [g_{N1} \quad g_{N2} \quad g_{N1A} \quad g_{N1B} \quad g_{N2A} \quad g_{N2B}]^{\mathrm{T}}, \tag{70}$$

$$\mathbf{W}_N = [\mathbf{w}_{N1} \quad \mathbf{w}_{N2} \quad \mathbf{w}_{N1A} \quad \mathbf{w}_{N1B} \quad \mathbf{w}_{N2A} \quad \mathbf{w}_{N2B}], \tag{71}$$

$$\bar{\mathbf{w}}_N = [\bar{w}_{N1} \quad \bar{w}_{N2} \quad \bar{w}_{N1A} \quad \bar{w}_{N1B} \quad \bar{w}_{N2A} \quad \bar{w}_{N2B}]^{\mathrm{T}}, \tag{72}$$

$$\hat{\mathbf{w}}_N = \mathbf{0}_{61}. \tag{73}$$

As friction is not taken into account, the closed contacts are always assumed to slip, which can be expressed by

$$\mathbf{W}_T = \mathbf{0}_{46}, \quad \hat{\mathbf{w}}_T = \mathbf{1}_{61}, \quad \bar{\mathbf{w}}_T = \mathbf{0}_{61}. \tag{74}$$

5.1. Results

For the numerical analysis of the tumbling toy, we consider the following data set:

Dynamics $m_S = 0.04$ kg, $J_S = 4.0833\,10^{-6}$ kg m^2, $m_B = 0.0225$ kg, $g = 9.81$ m/s^2;
Geometry $a = 0.0105$ m, $b = 0.002$ m, $l = 0.035$ m, $R = 0.0025$ m, $\varphi_R = \frac{1}{6}\pi$ rad, $\varphi_T = 0.28$ rad, $p = 0.025$ m, $s = p\tan(\varphi_T)$;
Contact $\mu = 0, \varepsilon_N = 0$.

The geometry and masses were measured and the inertias estimated. Friction and restitution were neglected because they are not essential for the operation of the toy and are estimated to be small, which corresponds to frictionless completely inelastic contacts. Using these parameters, the tumbling toy was simulated and a stable periodic solution was found. Although, in general, more stable periodic solutions can co-exist, this periodic solution is the only stable periodic solution for the current parameter set (as will be shown later), which corresponds with the intended operation of the toy. The time history of the coordinates of this periodic motion is depicted in Figure 16 for one period, i.e. one revolution of the body. The motion during the second part of the period is, of course, identical to the first part due to the symmetry in the system. It therefore suffices to consider only half-a-period.

The motion of the toy is too complicated to be fully understood from the time histories and the motion was therefore analyzed with a computer animation. Some frames of the animation are depicted in Figure 17. The numbers of the frames correspond to the numbers of the vertical dashed lines in Figure 16. Let t_k denote the time at frame k. At $t = t_1$ the body rotates around one pivot until the other pivot impacts with the rail ($t = t_2$). The body then starts moving forward ($t = t_3$) with pivots in contact with the rail and the ball starts rolling forward. The sliding direction of the body is reversed after some time ($t = t_4$) because the ball is still on the right side of the body. At $t = t_5$ the pivot on the upper teeth comes again in double contact with the rail, which cause the other pivot to detach. The ball, still moving forward, has at $t = t_6$ passed the center of the body, which causes the body to rotate forward again. After an impact of the lower pivot at $t = t_7$ and of the ball at $t = t_8$, the upper pivot slides over the tooth and the body is flipped over ($t = t_{10}$). The sequence of events is, of course, very dependent on the chosen parameter set, but the results of Figure 16 correspond well with what can be seen from the movement of the real toy although no real measurements have been carried out. The frequency of the simulated periodic motion is $f = 1.04$ Hz, which corresponds well with the observed frequency of 1.0 Hz.

The system has a set of (marginally) stable equilibria, all characterized by a double-point contact of one pivot with the rail and the ball in contact with the lowest point in the body. The equilibria are marginally stable because no damping or friction is modeled. As the system can rest at any tooth of the rail, and with pivot 1 or 2, there is a set of such equilibria. One of those stable equilibria, resting on pivot 2, is given by

$$
\begin{aligned}
x_S^{se} &= (p+R)\cos\varphi_T - R\sin\varphi_T + a\cos\varphi_S^{se} - b\sin\varphi_S^{se} \\
y_S^{se} &= (p+R)\sin\varphi_T + R\cos\varphi_T + a\sin\varphi_S^{se} + b\cos\varphi_S^{se}
\end{aligned}
$$

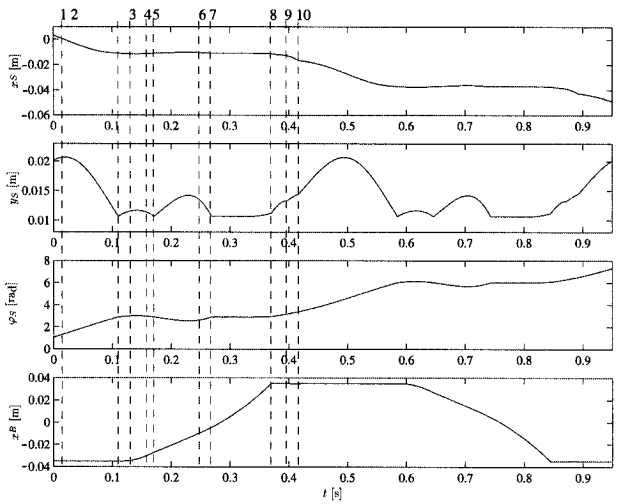

Figure 16. Time history of the coordinates of the tumbling toy.

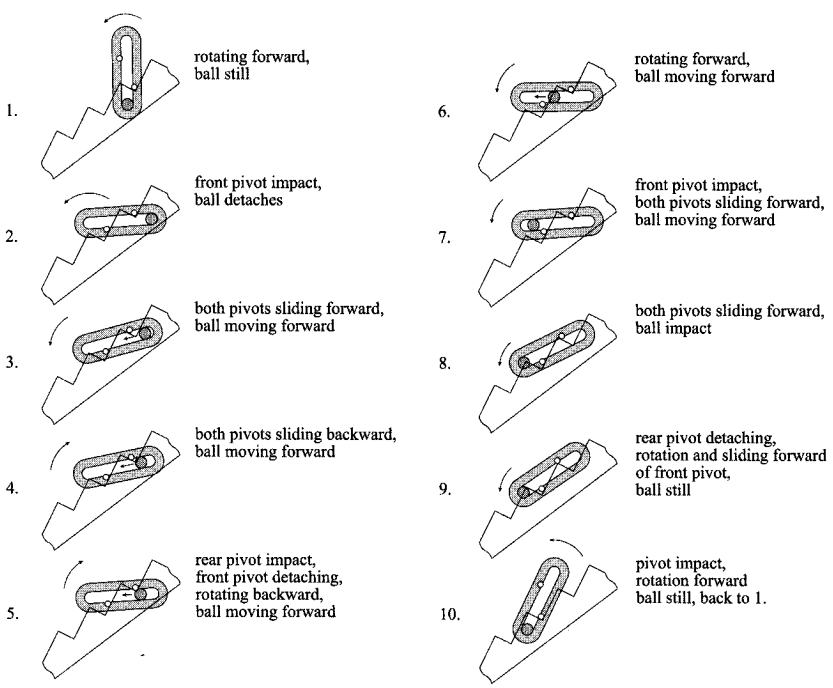

Figure 17. Sequence of events for the tumbling toy (arrows indicate velocity after impact).

$$\begin{aligned} \varphi_S^{se} &= \pi - \varphi_R + \arctan \frac{m_S a - m_B (l-a)}{b(m_S + m_B)} \\ x_B^{se} &= -l \end{aligned} \tag{75}$$

for which $g_{N2A} = 0, g_{N2B} = 0$ and $g_{N2} = 0$. Other equilibria are characterized by a resting position on pivot 1, with $g_{N1A} = 0, g_{N1B} = 0$ and $g_{N1} = 0$.

The body can assume a horizontal position, $\varphi_S + \varphi_R = \pi$, with double-point contact of one pivot with the rail, if the kinematic condition $\varphi_R + \varphi_T > \arccos \frac{s}{2c} - \arctan \frac{b}{a}$ holds. A horizontal position of the body allows for an unstable equilibrium, for which the body is balanced on one pivot by the moments $m_S a$ and $m_B (x_B - a)$. This unstable position is possible on every tooth and with pivot 1 or 2. Therefore, the system has a set of unstable equilibria for high enough values of φ_R. One of these unstable equilibria is given by

$$\begin{aligned} x_S^{ue} &= (p + R + a)\cos\varphi_T + (b - R)\sin\varphi_T \\ y_S^{ue} &= (p + R - a)\sin\varphi_T + (b + R)\cos\varphi_T \\ \varphi_S^{ue} &= \pi - \varphi_R \\ x_B^{ue} &= -(1 + \frac{m_S}{m_B})a \end{aligned} \tag{76}$$

for which $g_{N2A} = 0$ and $g_{N2B} = 0$. Other equilibria are characterized by a resting position on pivot 1, with $g_{N1A} = 0$ and $g_{N1B} = 0$ and $x_B^{ue} = (1 + \frac{m_S}{m_B})a$. The unstable equilibria are saddle points. Note that the toy is constructed such that $m_B (l - a) > m_S a$, to allow for a periodic motion of the toy.

The system has four degrees of freedom, which sets up an eight-dimensional state space $(\mathbf{q}, \dot{\mathbf{q}}) \in \mathbb{R}^8$. The accelerations $\ddot{\mathbf{q}}$ are dependent on $\mathbf{z} = (x_S \bmod p\cos\varphi_R, y_S, \varphi_S \bmod \pi, x_B, \dot{\mathbf{q}}) \in \mathbb{R}^8$ and not on the absolute displacement x_S and rotation φ_S. The on-average decreasing displacement x_S and increasing rotation φ_S can never be periodic. By a periodic solution of the system, we mean periodic motion of the states $\mathbf{z}$.

The motion of the system goes through states with simultaneous double contact of a pivot and contact of the ball, which allows for a one-dimensional Poincaré map. We define the section Σ

$$\begin{aligned} \Sigma = \{\mathbf{z} \in \mathbb{R}^8 \mid (&g_{N1A} = g_{N1B} = g_{N1} = \dot{g}_{N1A} = \dot{g}_{N1B} = \dot{g}_{N1} = 0 \vee \\ &g_{N2A} = g_{N2B} = g_{N2} = \dot{g}_{N2A} = \dot{g}_{N2B} = \dot{g}_{N2} = 0) \wedge \varphi_S = \varphi_S^{se} \wedge \dot{\varphi}_S > 0\}. \end{aligned} \tag{77}$$

For a state $\mathbf{z} \in \Sigma$ the only unknown is the velocity $\dot{\varphi}_S$. From a state $\mathbf{z} \in \Sigma$ with $\dot{\varphi}_S = \dot{\varphi}_{S_k}$, a solution evolves which may return to Σ. The return value of $\dot{\varphi}_S$ on Σ is denoted by $\dot{\varphi}_{S_{k+1}}$. We define the one-dimensional first return map $P : \Sigma \to \Sigma$ as

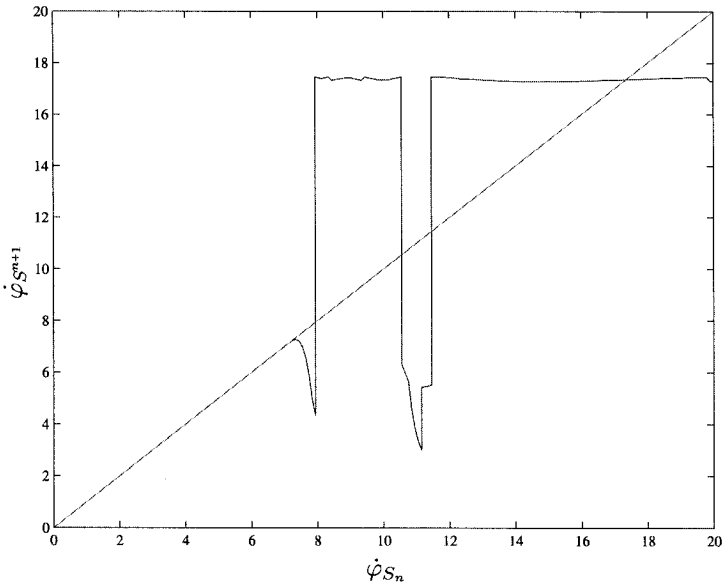

Figure 18. Poincaré map of the tumbling toy, $\varphi_R = \frac{\pi}{6}$ rad.

$$\dot{\varphi}_{S_{k+1}} = P(\dot{\varphi}_{S_k}). \tag{78}$$

Periodic solutions and equilibria, which pass the section Σ, are fixed points of P, i.e. they are regular crossings of the map P with the diagonal $\dot{\varphi}_{S_k} = \dot{\varphi}_{S_{k+1}}$. The set of stable equilibria appear therefore as a fixed point of the mapping P at $\dot{\varphi}_S = 0$. Small oscillations around the stable equilibrium point are undamped. These undamped oscillations, which we denote with marginally stable periodic solutions, are centers in the phase space, which explains why the mapping remains tangent to the diagonal for $0 < \dot{\varphi}_S < 7.1$. The set of unstable equilibria is not located on Σ and the unstable equilibria cannot therefore appear as regular crossings of the map P with the diagonal.

The Poincaré map P, for $\varphi_R = \frac{\pi}{6}$ is shown in Figure 18 together with the diagonal. The map has a regular crossing with the diagonal at $\dot{\varphi}_S = 17.3$ rad/s, which corresponds with the periodic solution depicted in Figure 16.

The oscillations around the stable equilibrium point become damped for $7.1 < \dot{\varphi}_{S_k} < 7.95$. The ball detaches for a short moment of time from the end of the body but almost immediately returns to the same contact point, which causes a slight dissipation. The mapping is lower than the diagonal due to this dissipation. It can be observed that the distance which the ball travels in the body increases with increasing values of $\dot{\varphi}_{S_k}$ as the dissipation increases.

At $\dot{\varphi}_S = 7.95$ the ball travels so far within the body that it reaches the unstable equilibrium position. For $7.95 < \dot{\varphi}_S < 10.55$ the ball will slam to the other end of the body and the body will begin to perform the periodic motion depicted in Figure 16. The map is therefore discontinuous at $\dot{\varphi}_S = 7.95$. The discontinuity is caused by the unstable equilibrium point, which is not located on Σ. The map appears to be discontinuous at various

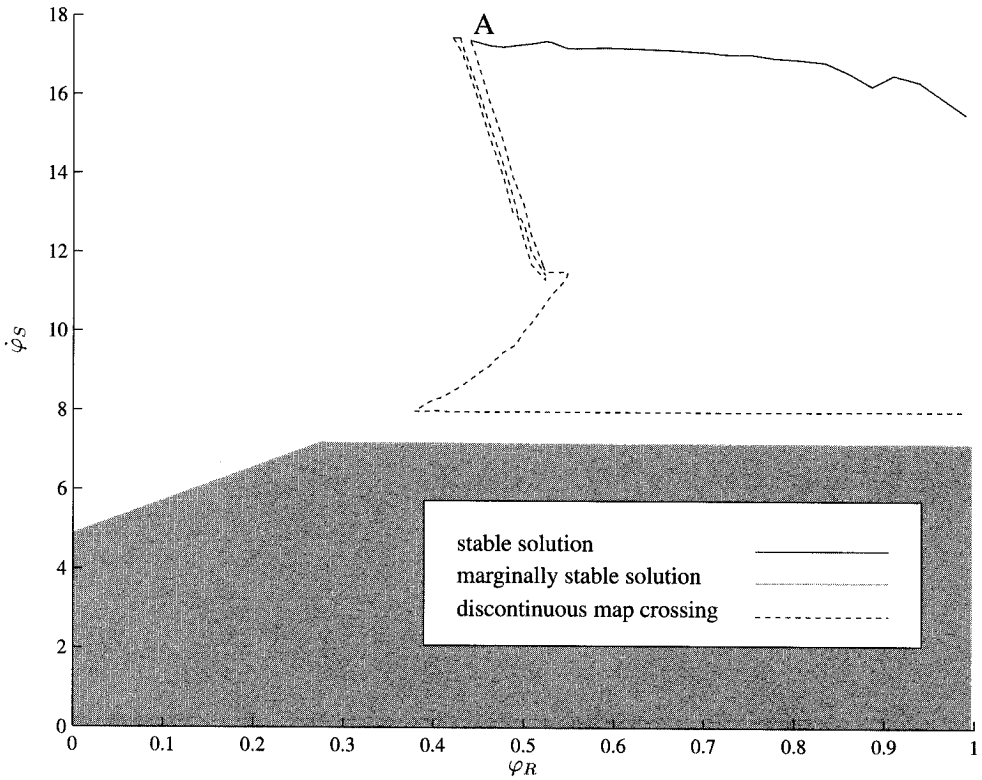

Figure 19. Bifurcation diagram of the tumbling toy.

values of $\dot{\varphi}_{S_k}$. Between $10.55 < \dot{\varphi}_{S_k} < 11.45$, the free pivot (the one on which the body is not rotating) hits the rail before the ball reaches the unstable equilibrium point, and the toy will not start the periodic motion but return to its stable equilibrium position. A small discontinuity can be observed at $\dot{\varphi}_{S_k} = 11.15$. The ball makes one impact before coming to rest for $\dot{\varphi}_{S_k} > 11.15$, whereas the ball makes two impacts for $\dot{\varphi}_{S_k} < 11.15$ (resulting in more dissipation). At $\dot{\varphi}_{S_k} = 11.45$ the free pivot hits the rail before the ball reaches the unstable equilibrium position, but the ball still manages to come to the other side after the impact between pivot and rail. Starting values with $\dot{\varphi}_{S_k} > 11.45$ will therefore lead to the periodic motion depicted in Figure 16.

The unstable equilibrium point is a saddle point, which causes neighbouring solutions to separate when they start at different sides of a separatrix of the saddle point. The discontinuities in the one-dimensional map are due to this separating effect of the saddle point. We observe that the discontinuities in the map can also cross the diagonal. The values of $\dot{\varphi}_{S_k}$ for which the map is discontinuous are, in fact, the intersection points of the separatrices of the saddle point with the section Σ.

Note that there is a similarity between the tumbling toy and the simple pendulum $\ddot{\theta} + 2\alpha\dot{\theta} + \sin\theta = \beta$ with external torque β ; see, for instance, Guckenheimer, and Holmes (1983). The basins of attraction of the stable equilibria and periodic solutions are separated

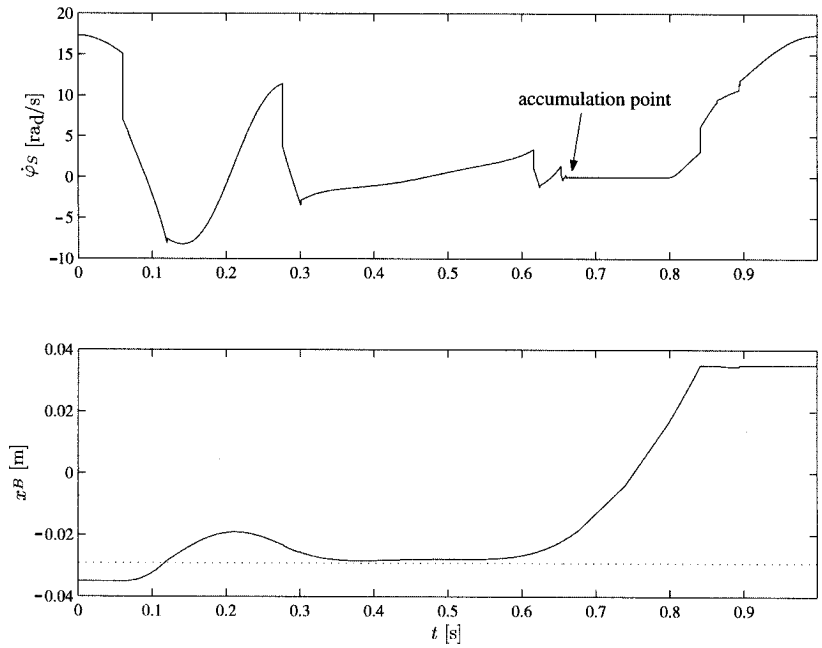

Figure 20. Periodic solution near bifurcation point A, $\varphi_R = 0.44$ rad.

for the simple pendulum by the saddle points and their separatrices. The tumbling toy shows a similar behavior although it is a multi-degree-of-freedom system, which makes the behavior more complicated.

The bifurcation diagram of the tumbling toy (Figure 19) was created by calculating 76 one-dimensional maps for varying values of φ_R. For $\varphi_R = \frac{\pi}{6}$ we observe a stable periodic solution, three discontinuous crossings of the map with the diagonal and a set of marginally stable periodic solutions (being the set of undamped oscillations around the equilibrium), which correspond with the crossings of the map with the diagonal in Figure 18.

The stable periodic solution approaches the unstable equilibrium point for decreasing values of φ_R and a homoclinic[2] bifurcation occurs at point A. The periodic solution near the bifurcation point is shown in Figure 20 and approaches the unstable equilibrium point at $x_B = -(1 + \frac{m_S}{m_B})a$ (indicated by the dotted line). The periodic solution is a homoclinic orbit exactly at the bifurcation point with an infinitely long period time because the periodic solution includes an equilibrium. The vector field is smooth in the neighborhood around the saddle point. The bifurcation point has therefore to be understood as a conventional bifurcation point. Note that the discontinuity crossings of the map are due to the separatrices of the saddle point and not due to the non-smoothness of the system.

Another peculiarity of the periodic solution shown in Figure 20 is the existence of an accumulation point within the periodic solution. At an accumulation point, an infinitely large number of mode switches (in this case impacts) occur in a finite time. The toy rocks on the two pivots and the body comes to rest while the ball is rolling to the other side. The tumbling toy is similar to the rocking rod system (Glocker, 1995; Pfeiffer and Glocker, 1996). The

rocking rod system consists of a rod which can be in contact with two equidistant unilateral supports. If the rod is released such that it is in contact with one of the supports, then it can come to rest at the two supports with one impact. For a certain parameter range however, the rod will rock on the supports and will come to rest with an infinitely large number of impacts in a finite time. Rocking will occur when $J_S > ma^2$, where J_S and m are the mass and inertia of the rod and $2a$ is the distance between the supports. Similarly, the tumbling toy can rock on the two pivots, although it is more complicated due to the shape of the rail and the additional degree of freedom of the ball.

6. THE WADDLING DUCK

The waddling duck, depicted in Figure 21, is a toy which "walks" down an inclined slope with a forward–backward rocking motion. The toy consists of a body with a body-fixed front leg and a freely rotating rear leg, which is hinged to the body. The toy will be modeled with four degrees of freedom $\mathbf{q} = [x_S \quad y_S \quad \varphi_S \quad \varphi_B]^{\mathrm{T}}$, where x_S, y_S and φ_S are the displacements and rotation of the center of gravity of the body S with respect to the inclined slope. The angle of the rear leg relative to the slope is denoted by φ_B. The rotation of the rear leg is constrained by the front leg and a stop, $0 \leq \varphi_B - \varphi_S \leq \varphi_c$. The center of gravity of the rear leg is point B, which is located at a distance l_B from the hinge. The legs have an identical (mirrored) shape. The feet have a tread described by a circle segment with radius R. Sliding motion is observed in the actual toy and friction will therefore be taken into account. No restitution after impact is observed for the actual toy. The impacts will therefore be modeled as completely inelastic, $\varepsilon = 0$.

The mass matrix $\mathbf{M}$ and force vector $\mathbf{h}$ can be derived in a straightforward manner. They are

$$\mathbf{M} = \begin{bmatrix} (m_S + m_B) & 0 & m_B D_2 & m_B l_B \cos\varphi_B \\ 0 & (m_S + m_B) & m_B D_1 & m_B l_B \sin\varphi_B \\ m_B D_2 & m_B D_1 & (J_S + m_B (c^2 + d^2)) & m_B l_B E_2 \\ m_B l_B \cos\varphi_B & m_B l_B \sin\varphi_B & m_B l_B E_2 & (J_B + m_B l_B^2) \end{bmatrix} \tag{79}$$

$$\mathbf{h} = \begin{bmatrix} m_B D_1 \dot{\varphi}_S^2 + m_B l_B \sin\varphi_B \dot{\varphi}_B^2 - (m_S + m_B) g_x \\ -m_B D_2 \dot{\varphi}_S^2 - m_B l_B \cos\varphi_B \dot{\varphi}_B^2 - (m_S + m_B) g_y \\ m_B l_B E_1 \dot{\varphi}_B^2 - m_B (D_2 g_x + D_1 g_y) \\ -m_B l_B E_1 \dot{\varphi}_S^2 - m_B l_B (g_x \cos\varphi_B + g_y \sin\varphi_B) \end{bmatrix}. \tag{80}$$

Here, we use the abbreviations $d = 2a - b$, $D_1 = d\cos\varphi_S + c\sin\varphi_S$, $D_2 = -d\sin\varphi_S + c\cos\varphi_S$, $E_1 = D_2 \sin\varphi_B - D_1 \cos\varphi_B$ and $E_2 = D_2 \cos\varphi_B + D_1 \sin\varphi_B$. Furthermore, we introduce the following abbreviations:

$$F_1 = -(L + c - R)\cos\varphi_S - (b - a)\sin\varphi_S,$$

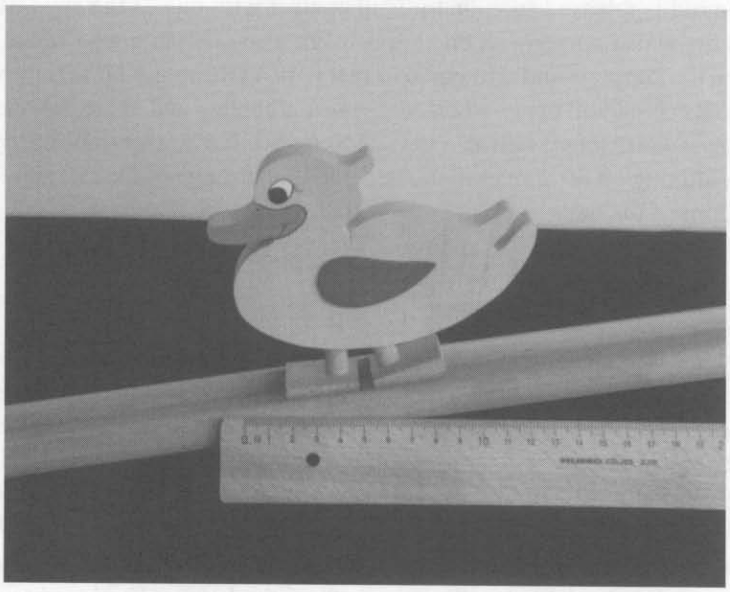

Figure 21. The waddling duck toy.

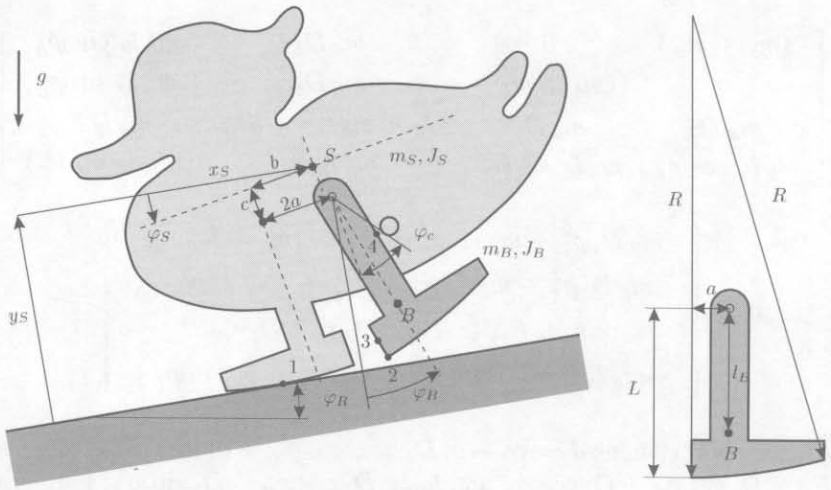

Figure 22. Model of the waddling duck toy.

$$
\begin{aligned}
F_2 &= (L+c-R)\sin\varphi_S - (b-a)\cos\varphi_S, \\
G_1 &= -(L+c)\cos\varphi_S - (b-a)\sin\varphi_S, \quad G_2 = (L+c)\sin\varphi_S - (b-a)\cos\varphi_S, \\
H_1 &= -a\sin\varphi_B - L\cos\varphi_B, \quad H_2 = -a\cos\varphi_B + L\sin\varphi_B, \\
I_1 &= -a\sin\varphi_B - (L-R)\cos\varphi_B, \quad I_2 = -a\cos\varphi_B + (L-R)\sin\varphi_B.
\end{aligned} \tag{81}
$$

It holds that $\dot{D}_1 = D_2\dot{\varphi}_S$, $\dot{D}_2 = -D_1\dot{\varphi}_S$, $\dot{E}_1 = E_2(\dot{\varphi}_B - \dot{\varphi}_S)$, $\dot{E}_2 = -E_1(\dot{\varphi}_B - \dot{\varphi}_S)$, $\dot{F}_1 = F_2\dot{\varphi}_S$, $\dot{F}_2 = -F_1\dot{\varphi}_S$, $\dot{G}_1 = G_2\dot{\varphi}_S$, $\dot{G}_2 = -G_1\dot{\varphi}_S$, $\dot{H}_1 = H_2\dot{\varphi}_B$, $\dot{H}_2 = -H_1\dot{\varphi}_B$, $\dot{I}_1 = I_2\dot{\varphi}_B$, $\dot{I}_2 = -I_1\dot{\varphi}_B$.

The contact distance g_{N1} is the smallest distance between the tread of the fixed front leg and the slope. The closest point on the tread to the slope is a regular point on the circle segment when $\varphi_S > 0$, or the right corner of the foot when $\varphi_S \leq 0$. The toy is assumed not to tumble forward nor backward, $|\varphi_S| \ll 1$. The contact distances in the normal and tangential directions of the front leg are

$$
g_{N1} = \begin{cases} y_S + F_1 - R, & \varphi_S > 0 \\ y_S + G_1, & \varphi_S \leq 0 \end{cases}, \tag{82}
$$

$$
g_{T1} = \begin{cases} x_S + F_2 + R\varphi_S, & \varphi_S > 0 \\ x_S + G_2, & \varphi_S \leq 0 \end{cases}. \tag{83}
$$

The tread of the rear leg is at a distance g_{N2} from the slope with tangential contact distance g_{T2}:

$$
g_{N2} = \begin{cases} y_S - D_2 + H_1, & \varphi_B \geq 0 \\ y_S - D_2 + I_1 - R, & \varphi_B < 0 \end{cases} \tag{84}
$$

$$
g_{T2} = \begin{cases} x_S + D_1 + H_2, & \varphi_B \geq 0 \\ x_S + D_1 + I_2 + R\varphi_B, & \varphi_B < 0 \end{cases}. \tag{85}
$$

The rotation of the rear leg is constrained by contact points 3 (the front leg) and 4 (the stop) with contact distances $g_{N3} = \varphi_B - \varphi_S$ and $g_{N4} = \varphi_c + \varphi_S - \varphi_B$.

From the contact distances $\mathbf{g}_N = [g_{N1} \quad g_{N2} \quad g_{N3} \quad g_{N4}]^{\mathrm{T}}$ we derive the contact vectors:

$$
\mathbf{w}_{N1} = \begin{cases} [0 \quad 1 \quad F_2 \quad 0]^{\mathrm{T}}, & \varphi_S > 0 \\ [0 \quad 1 \quad G_2 \quad 0]^{\mathrm{T}}, & \varphi_S \leq 0 \end{cases}, \quad \bar{w}_{N1} = \begin{cases} -F_2\dot{\varphi}_S^2, & \varphi_S > 0 \\ -G_2\dot{\varphi}_S^2, & \varphi_S \leq 0 \end{cases} \tag{86}
$$

$$\mathbf{w}_{T1} = \begin{cases} [1 \quad 0 \quad -F_1+R \quad 0]^{\mathrm{T}}, & \varphi_S > 0 \\ [1 \quad 0 \quad -G_1 \quad 0]^{\mathrm{T}}, & \varphi_S \leq 0 \end{cases}, \quad \bar{w}_{T1} = \begin{cases} -F_2\dot{\varphi}_S^2, & \varphi_S > 0 \\ -G_2\dot{\varphi}_S^2, & \varphi_S \leq 0 \end{cases} \tag{87}$$

$$\mathbf{w}_{N2} = \begin{cases} [0 \quad 1 \quad D_1 \quad H_2]^{\mathrm{T}}, & \varphi_B \geq 0 \\ [0 \quad 1 \quad D_1 \quad I_2]^{\mathrm{T}}, & \varphi_B < 0 \end{cases}, \quad \bar{w}_{N2} = \begin{cases} D_2\dot{\varphi}_S^2 - H_1\dot{\varphi}_B^2, & \varphi_B \geq 0 \\ D_2\dot{\varphi}_S^2 - I_1\dot{\varphi}_B^2, & \varphi_B < 0 \end{cases} \tag{88}$$

$$\mathbf{w}_{T2} = \begin{cases} [1 \quad 0 \quad D_2 \quad -H_1]^{\mathrm{T}}, & \varphi_B \geq 0 \\ [1 \quad 0 \quad D_2 \quad -I_1+R]^{\mathrm{T}}, & \varphi_B < 0 \end{cases},$$

$$\bar{w}_{T2} = \begin{cases} -D_1\dot{\varphi}_S^2 - H_2\dot{\varphi}_B^2, & \varphi_B \geq 0 \\ -D_1\dot{\varphi}_S^2 - I_2\dot{\varphi}_B^2, & \varphi_B < 0 \end{cases} \tag{89}$$

$$\mathbf{w}_{N3} = [0 \quad 0 \quad -1 \quad 1]^{\mathrm{T}}, \quad \bar{w}_{N3} = 0 \tag{90}$$

$$\mathbf{w}_{N4} = [0 \quad 0 \quad 1 \quad -1]^{\mathrm{T}}, \quad \bar{w}_{N4} = 0 \tag{91}$$

$$\hat{w}_{N1} = \hat{w}_{N2} = \hat{w}_{N3} = \hat{w}_{N4} = 0 \tag{92}$$

$$\hat{w}_{T1} = \hat{w}_{T2} = \hat{w}_{T3} = \hat{w}_{T4} = 0. \tag{93}$$

6.1. Results

For the numerical analysis of the waddling duck, we consider the following data set:

Dynamics $m_B = 0.010\,\mathrm{kg}, J_B = 1.0\,10^{-6}\,\mathrm{kg\,m^2}, m_S = 0.080\,\mathrm{kg}, J_S = 1.5\,10^{-4}\,\mathrm{kg\,m^2}$, $g = 9.81\,\mathrm{m/s^2}$;

Geometry $a = 0.006$ m, $b = 0.012$ m, $c = 0.005$ m, $l_B = 0.040$ m, $R = 0.100$ m, $L = 0.050$ m, $\varphi_R = \frac{\pi}{20}$ rad, $\varphi_c = 0.17$ rad;

Contact $\mu = 0.3, \varepsilon = 0$, for all contact points.

The geometry and masses were measured and the inertias were estimated. The contacts are regarded to be completely inelastic as no restitution was observed. The friction coefficient was measured to be approximately equal to 0.3. A stable periodic solution was found for the above data set, which corresponds to the intended operation of the toy. The time history of the coordinates $\mathbf{q}$ and normal contact distances $\mathbf{g}_N$ is shown in Figure 23 for one period. The motion is clarified by Figure 24. The numbers of the frames correspond to the numbers in Figure 23. The toy rolls from its front leg to its rear leg and back and takes a step each time the front leg impacts with the slope while standing on the rear leg. The rear leg is subsequently

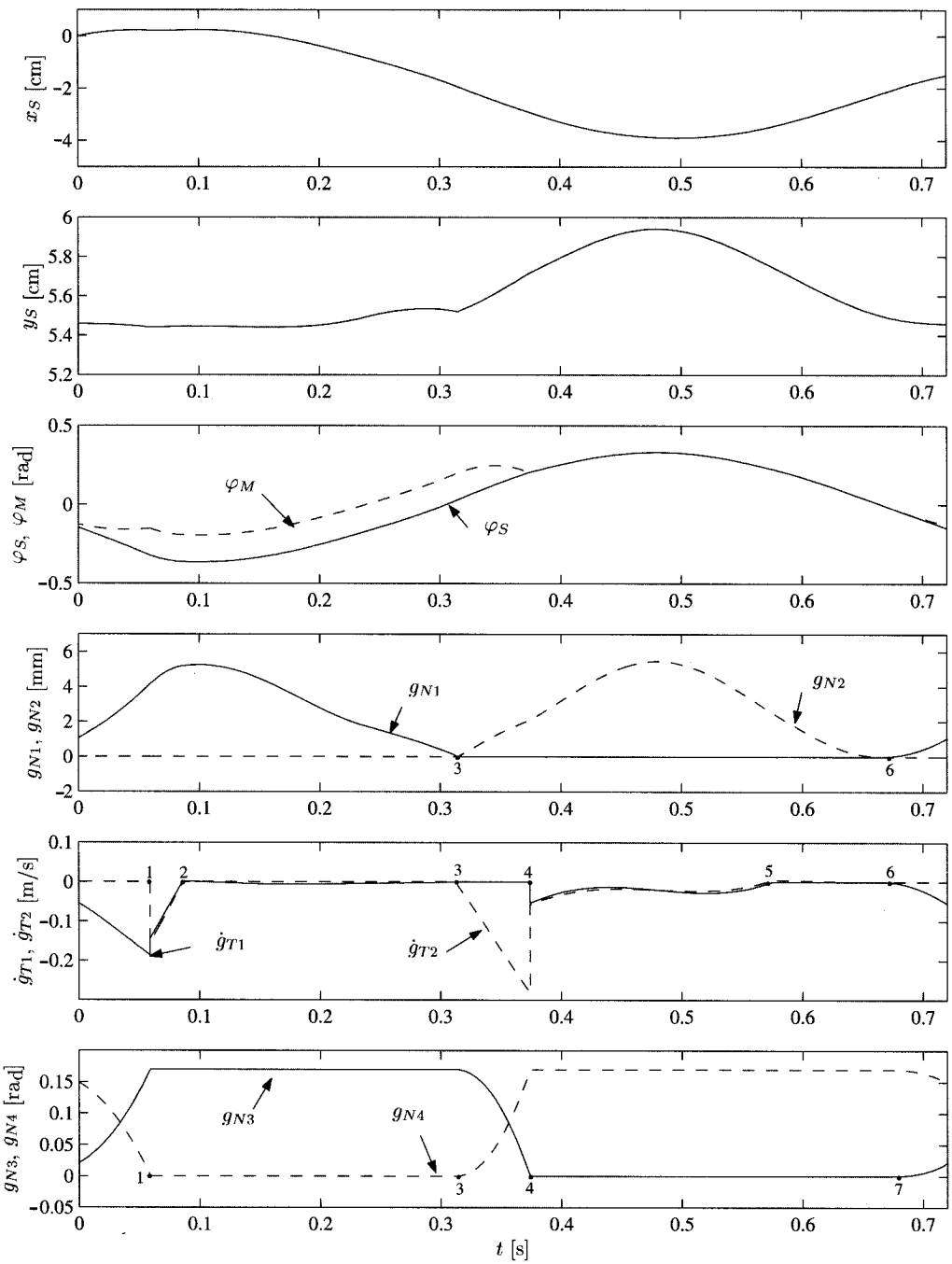

Figure 23. Time history of the coordinates.

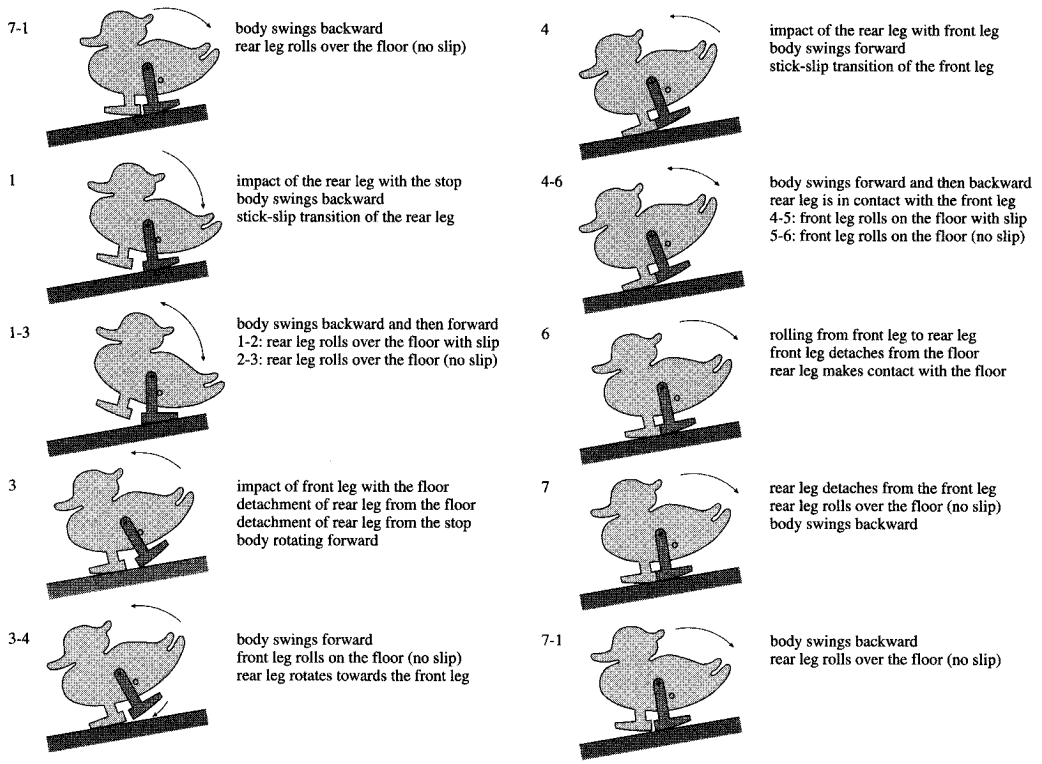

Figure 24. Sequence of events for the waddling duck.

closed to the front leg while rolling forward on the front leg. The gap between the rear leg and front leg (contact 3) opens again when the toy rolls backward on the rear leg.

6.2. Equilibria

Testing the toy when standing still for different angles of the inclination φ_R of the slope reveals that the toy has a rich bifurcation behavior of the equilibria. The toy is able to stand still on its front leg, or on its rear leg, or on both legs for a certain parameter range. The analysis of the equilibria is complicated by the non-smoothness of the feet, as a foot can make contact with the slope with its non-smooth corner point or with a regular point on the smooth circular part of the tread. The constraints on the rotation of the rear leg relative to the front leg, imposed by contacts 3 and 4, enlarge the number of structural possibilities even more. Each structural type of equilibrium constitutes a branch in the bifurcation diagram with variation of φ_R.

6.2.1. Branch: $g_{N3} = 0$

The waddling duck has, for large enough values of φ_R and μ, a stable equilibrium[3] for which the duck is resting on the front leg ($g_{N1} = 0$) or rear leg ($g_{N2} = 0$) and with the rear leg

closed to the front leg ($g_{N3} = \varphi_S - \varphi_B = 0$). The mass of the body m_S balances for this equilibrium the mass of the rear leg m_B around the contact point of the front leg with the slope:

$$\begin{aligned} & m_S \left(-R\sin\varphi_R + (R-L-c)\sin(\varphi_S^{\mathrm{r3}} + \varphi_R) + (a-d)\cos(\varphi_S^{\mathrm{r3}} + \varphi_R)\right) \\ = \; & m_B \left(R\sin\varphi_R - (R-L+l_B)\sin(\varphi_S^{\mathrm{r3}} + \varphi_R) - a\cos(\varphi_S^{\mathrm{r3}} + \varphi_R)\right) \end{aligned} \tag{94}$$

After some deduction we can express the angle of the body φ_S^{r3} as

$$\varphi_S^{\mathrm{r3}} = -\arccos\left(\frac{A}{\sqrt{A^2+B^2}}\right) + \arcsin\left(\frac{C}{\sqrt{A^2+B^2}}\right) - \varphi_R \tag{95}$$

with

$$\begin{aligned} A &= (m_S + m_B)(R-L) - m_S c + m_B l_B, \\ B &= m_S(a-d) + m_B a, \\ C &= (m_S + m_B)R\sin\varphi_R. \end{aligned} \tag{96}$$

The equilibrium can exist when φ_R is large enough such that $\lambda_{N3} > 0$ ($g_{N3} = 0$ remains satisfied). From the condition $\lambda_{N3} > 0$ it follows that $\varphi_S^{\mathrm{r3}} + \varphi_R > 0$, which sets a lower bound to φ_R given by

$$\varphi_R^{gN3} = \arcsin\frac{(m_S + m_B)a - m_S d}{(m_S + m_B)R}. \tag{97}$$

The duck will rest on the front leg for $\varphi_S^{\mathrm{r3}} > 0$ and on the rear leg for $\varphi_S^{\mathrm{r3}} < 0$, which gives another critical value given by

$$\varphi_R^{S0} = \arctan\frac{(m_S + m_B)a - m_S d}{(m_S + m_B)L + m_S c - m_B l_B}. \tag{98}$$

For very large values of φ_R, the body will start to slip. The upper bound of φ_R is therefore given by

$$\varphi_R^{\mathrm{slip}} = \arctan\mu. \tag{99}$$

For practical values of $c < L < R$, $\varphi_R^{gN3} < \varphi_R^{S0}$ holds. The stable equilibrium, with a closed rear leg and resting on the front leg, exists when $\varphi_R^{S0} < \varphi_R < \varphi_R^{\mathrm{slip}}$. The stable equilibrium, with a closed rear leg and resting on the rear leg, exists when $\varphi_R^{gN3} < \varphi_R < \varphi_R^{S0}$.

6.2.2. Branch $g_{N2} = 0, g_{N4} = 0$

For small enough values of φ_R, stable and unstable equilibria can exist for which the duck is resting on the rear leg ($g_{N2} = 0$) and for which the legs are fully parted $g_{N4} = 0$. The contact point between foot and slope is a regular point for $\varphi_B < 0$ and the corner of the foot for $\varphi_B \geq 0$. The equilibrium with $\varphi_B < 0$ is characterized by a balance between mass m_S and m_B around contact point 2:

$$\begin{aligned} & m_S \left(-R\sin\varphi_R + (R-L)\sin(\varphi_B^{\mathrm{r}24} + \varphi_R) + a\cos(\varphi_B^{\mathrm{r}24} + \varphi_R)\right. \\ - \quad & \left. d\cos(\varphi_S^{\mathrm{r}24} + \varphi_R) - c\sin(\varphi_S^{\mathrm{r}24} + \varphi_R)\right) \\ = \quad & m_B \left(R\sin\varphi_R - (R-L+l_B)\sin(\varphi_B^{\mathrm{r}24} + \varphi_R) - a\cos(\varphi_B^{\mathrm{r}24} + \varphi_R)\right). \end{aligned} \tag{100}$$

We can express the angle of the body $\varphi_S^{\mathrm{r}24}$ as

$$\varphi_S^{\mathrm{r}24} = -\arccos\left(\frac{A}{\sqrt{A^2+B^2}}\right) + \arcsin\left(\frac{C}{\sqrt{A^2+B^2}}\right) - \varphi_R \tag{101}$$

with

$$\begin{aligned} A &= ((m_S + m_B)(R-L) + m_B l_B)\cos\varphi_c - (m_S + m_B)a\sin\varphi_c - m_S c, \\ B &= ((m_S + m_B)(R-L) + m_B l_B)\sin\varphi_c + (m_S + m_B)a\cos\varphi_c - m_S d, \\ C &= (m_S + m_B)R\sin\varphi_R. \end{aligned} \tag{102}$$

The rotation of the rear leg follows from $g_{N4} = 0$ and is $\varphi_B^{\mathrm{r}24} = \varphi_S^{\mathrm{r}24} + \varphi_c$. The stable equilibrium on the rear leg can only exist when $\varphi_B^{\mathrm{r}24} < 0$ which sets an upper bound φ_R^{B0} to φ_R

$$\varphi_R^{B0} = \arctan\frac{(m_S + m_B)a - m_S d\cos\varphi_c + m_S c\sin\varphi_c}{(m_S + m_B)L - m_B l_B + m_S d\sin\varphi_c + m_S c\cos\varphi_c}. \tag{103}$$

The condition

$$-d\cos(\varphi_S^{\mathrm{sr}} + \varphi_R) - c\sin(\varphi_S^{\mathrm{sr}} + \varphi_R) > 0 \tag{104}$$

must hold to assure a positive contact force λ_{N4}. From this condition follows (after some deductions) another upper bound of φ_R:

$$\varphi_R^{gN4} = \arcsin\frac{(R-L+l_B\frac{m_B}{m_S+m_B})(c\sin\varphi_c - d\cos\varphi_c) + a(c\cos\varphi_c + d\sin\varphi_c)}{R\sqrt{c^2+d^2}}. \tag{105}$$

The stable equilibrium, resting on the rear leg with $g_{N4} = 0$, exists when $\varphi_R < \varphi_R^{B0} \wedge \varphi_R < \varphi_R^{gN4} \wedge \varphi_R < \varphi_R^{\mathrm{slip}}$. For the current parameter set, $\varphi_R^{B0} < \varphi_R^{gN4} < \varphi_R^{\mathrm{slip}}$ holds. This branch

folds around at $\varphi_R = \varphi_R^{B0}$ and proceeds as an unstable branch. The equilibria on the unstable branch are characterized by $g_{N2} = g_{N4} = 0$ and $\varphi_B > 0$. The balance of masses m_S and m_B around contact point 2 yields the condition

$$\begin{aligned} & m_S \left(-L\sin(\varphi_B^{c24}+\varphi_R)+a\cos(\varphi_B^{c24}+\varphi_R)\right. \\ - \quad & \left. d\cos(\varphi_S^{c24}+\varphi_R)-c\sin(\varphi_S^{c24}+\varphi_R)\right) \\ = \quad & m_B \left(L\sin(\varphi_B^{c24}+\varphi_R)-a\cos(\varphi_B^{c24}+\varphi_R)\right). \end{aligned} \tag{106}$$

We can express the angle of the body φ_B^{c24} as

$$\varphi_B^{c24} = \arctan\left(\frac{(m_S+m_B)a - m_S d\cos(\varphi_c) + m_S c\sin(\varphi_c)}{(m_S+m_B)L - m_B l_B + m_S d\sin(\varphi_c) + m_S c\cos(\varphi_c)}\right) - \varphi_R. \tag{107}$$

The rotation of the front leg follows from $g_{N4} = 0$ and is $\varphi_S^{c24} = \varphi_B^{c24} - \varphi_c$.

6.2.3. Branch $g_{N2} = 0$, $g_{N3} > 0$ and $g_{N4} > 0$

An unstable equilibrium can exist with $g_{N2} = 0$, $g_{N3} > 0$ and $g_{N4} > 0$ for a certain parameter range. The unstable equilibrium is characterized by a resting position on the rear leg ($g_{N2} = 0$) and by a rotation of the body such that $-d\cos(\varphi_S^{sr}+\varphi_R)-c\sin(\varphi_S^{sr}+\varphi_R) = 0$. The center of mass of the body S is, for this rotation, located right above the hinge of the rear leg (which is an unstable position). The equilibrium has a regular contact point for $\varphi_B < 0$ and a non-smooth contact point for $\varphi_B \geq 0$. We can express the angle of the rear leg at the unstable equilibrium φ_B^{r2} for $\varphi_B < 0$ as

$$\varphi_B^{r2} = -\arccos\left(\frac{A}{\sqrt{A^2+B^2}}\right) + \arcsin\left(\frac{C}{\sqrt{A^2+B^2}}\right) - \varphi_R \tag{108}$$

with

$$\begin{aligned} A &= (m_S+m_B)(R-L)+m_B l_B, \\ B &= (m_S+m_B)a, \\ C &= (m_S+m_B)R\sin\varphi_R. \end{aligned} \tag{109}$$

The rotation of the body φ_S^{r2} can be expressed as

$$\varphi_S^{r2} = -\varphi_R - \arctan\frac{d}{c}. \tag{110}$$

The conditions $g_{N3} > 0$ and $g_{N4} > 0$ must hold for the unstable equilibrium to exist. The condition $g_{N3} > 0$ is violated when $\varphi_R \leq \varphi_R^{gN3}$ and the condition $g_{N4} > 0$ is violated when $\varphi_R \geq \varphi_R^{gN4}$. The branch turns around at $\varphi_B^{\mathrm{r}2} = 0$ and proceeds as $\varphi_B^{\mathrm{c}2}$ with the corner point as a contact point. The upper bound $\varphi_R^{\mathrm{B}02}$ to φ_R, for which $\varphi_B^{\mathrm{r}2} = 0$, is given by

$$\varphi_R^{B02} = \arctan \frac{(m_S + m_B)a}{(m_S + m_B)L - m_B l_B}. \tag{111}$$

The branch characterized by contact on the corner point is given by

$$\varphi_B^{c2} = \arctan \frac{(m_S + m_B)a}{(m_S + m_B)L - m_B l_B} - \varphi_R \tag{112}$$

for which $\varphi_B^{\mathrm{c}2} \geq 0$.

6.2.4. Set of equilibria with $g_{N1} = g_{N2} = 0$

All the previous equilibria were characterized by a single contact point, either resting on the front or the rear leg. Also, equilibria can exist which have a double contact point, i.e. both legs are in contact with the slope $g_{N1} = g_{N2} = 0$. The duck can, for certain values of φ_R, find a stable equilibrium for a range of values of $\varphi_B - \varphi_S$ within $0 \leq \varphi_B - \varphi_S \leq \varphi_c$. This type of equilibria is therefore troublesome as it does not constitute a branch but an area in the bifurcation diagram. The double-point equilibria can only exist for positive contact forces $\lambda_{N1} \geq 0$ and $\lambda_{N2} \geq 0$. The area in the bifurcation diagram has three edges defined by $\varphi_B - \varphi_S = \varphi_c$, $\lambda_{N1} = 0$ and $\lambda_{N2} = 0$.

It must hold for all equilibria within the area that $g_{N1} = g_{N2} = 0$, which can only be true for $\varphi_S > 0$ and $\varphi_B > 0$:

$$g_{N1} = y_S + F_1 - R = 0, \quad g_{N2} = y_S - D_2 + H_1 = 0. \tag{113}$$

This gives a relation between φ_S and φ_B after elimination of y_S

$$(L - R)\cos\varphi_S + a\sin\varphi_S + R - a\sin\varphi_B - L\cos\varphi_B = 0. \tag{114}$$

Evaluating the previous equation numerically reveals that $\varphi_S \ll \varphi_B \ll 1$, which allows for a Taylor approximation in φ_S, φ_B and φ_B^2:

$$\varphi_S = \varphi_B - \frac{L}{2a}\varphi_B^2 + O(\varphi_S^2) + O(\varphi_B^3). \tag{115}$$

For $\varphi_B - \varphi_S = 0$, it must hold that $\varphi_S = \varphi_B = 0$. The edge $\varphi_B - \varphi_S = \varphi_c$ is given by $\varphi_B = \sqrt{\frac{2a\varphi_c}{L}}$ and $\varphi_S = \sqrt{\frac{2a\varphi_c}{L}} - \varphi_c$.

The contact force λ_{N1} vanishes when

$$
\begin{aligned}
& m_S\,(-L\sin(\varphi_B+\varphi_R)+a\cos(\varphi_B+\varphi_R)\\
-\;& d\cos(\varphi_S+\varphi_R)-c\sin(\varphi_S+\varphi_R))\\
+\;& m_B\,((-L+l_B)\sin(\varphi_B+\varphi_R)+a\cos(\varphi_B+\varphi_R))\;=\;0. \qquad (116)
\end{aligned}
$$

The approximation of the above expression in first-order and second-order terms of φ_B together with equation (115) gives an expression for φ_B on the edge $\lambda_{N1}=0$

$$\varphi_B=\frac{B-\sqrt{B^2-4AC}}{2A} \qquad (117)$$

with

$$
\begin{aligned}
A &= m_S c\frac{L}{2a}-\frac{1}{2}((m_S+mB)a-m_S d),\\
B &= -(m_S+m_B)L+m_B l_B-m_S c-((m_S+m_B)a-m_S d)\varphi_R,\\
C &= (-(m_S+m_B)L+m_B l_B-m_S c)\varphi_R+(m_S+m_B)a-m_S d\\
&\quad -\frac{1}{2}((m_S+mB)a-m_S d)\varphi_R^2. \qquad (118)
\end{aligned}
$$

The second root (with a + sign) yields non-physical values of $\varphi_B-\varphi_S$ which have to be between 0 and φ_c.

The contact force λ_{N2} vanishes when

$$
\begin{aligned}
& m_S\,(-R\sin\varphi_R+(R-L-c)\sin(\varphi_S+\varphi_R)+(a-d)\cos(\varphi_S+\varphi_R))\\
+\;& m_B\,(-R\sin\varphi_R+(R-L)\sin(\varphi_S+\varphi_R)+a\cos(\varphi_S+\varphi_R)\\
+\;& l_B\sin(\varphi_B+\varphi_R))\;=\;0. \qquad (119)
\end{aligned}
$$

The approximation of the above expression in first-order and second-order terms of φ_B together with equation (115) gives an expression for φ_B

$$\varphi_B=\frac{B\pm\sqrt{B^2-4AC}}{2A} \qquad (120)$$

with

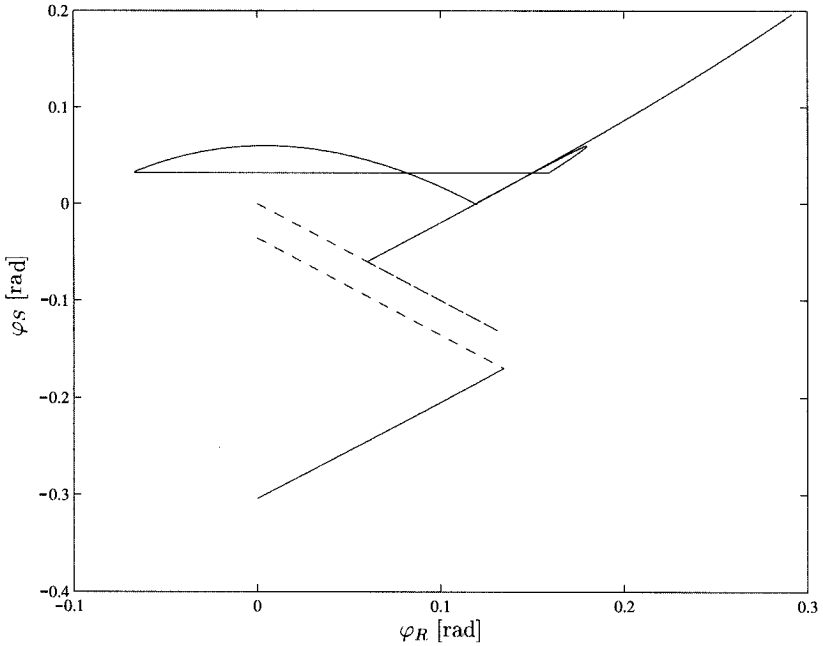

Figure 25. Equilibria of the waddling duck.

$$
\begin{aligned}
A &= -\frac{L}{2a}((m_S + m_B)(R-L) - m_S c) - \frac{1}{2}((m_S + mB)a - m_S d), \\
B &= (m_S + m_B)(R-L) + m_B l_B - m_S c - ((m_S + m_B)a - m_S d)\varphi_R, \\
C &= (-(m_S + m_B)L + m_B l_B - m_S c)\varphi_R + (m_S + m_B)a - m_S d \\
&\quad - \frac{1}{2}((m_S + mB)a - m_S d)\varphi_R^2 .
\end{aligned} \tag{121}
$$

where both roots contribute to the edge $\lambda_{N2} = 0$.

The values of φ_S of the equilibria of the waddling duck, as have been derived above, are depicted in Figure 25 for varying values of φ_R. Black lines indicate stable equilibria and dashed lines denote unstable equilibria. A schematic diagram of the equilibria is depicted in Figure 26 to clarify the branches in Figure 25. The set of equilibria with double contact is represented by the gray area. This area appears to be folded in the bifurcation diagram due to the projection in the φ_S direction (projection in the $\varphi_B - \varphi_S$ direction would yield a simple connected region). The dotted gray lines in Figure 26 do not represent branches of equilibria but show how the branches $g_{N2} = 0, \varphi_B > 0$ and $g_{N2} = g_{N4} = 0, \varphi_B < 0$ are directed towards the same point for which $\lambda_{N4} = 0$. The saddle–node bifurcations, at which the

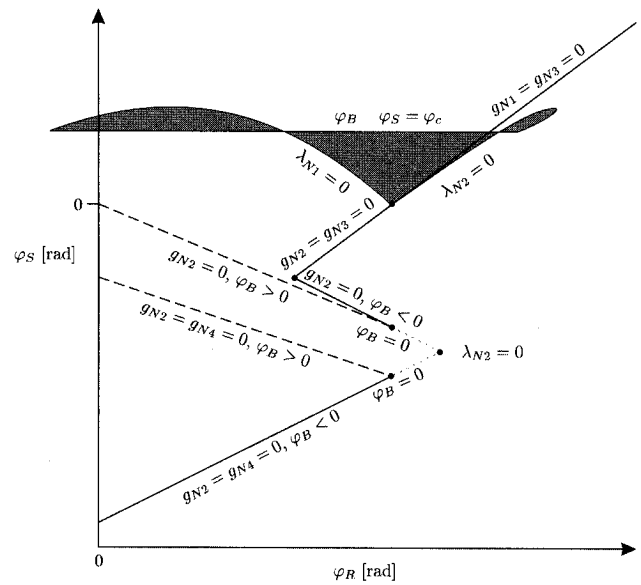

Figure 26. Sketch of the equilibria of the waddling duck.

branches turn around, are clearly non-conventional and are due to the non-smoothness of the system. The bifurcation points are sharp as opposed to smooth bifurcation points in a smooth system. Sharp bifurcation points of the equilibria are not necessarily caused by impact or friction but already occur in non-smooth systems $\dot{\mathbf{x}} = \mathbf{f}(\mathbf{x})$ which are continuous in the state vector $\mathbf{x}$ (Leine et al., 2000; Leine, 2000).

We observe that the system has only one equilibrium for $\varphi_R = \frac{\pi}{20}$, being the stable equilibrium resting on the front leg with $g_{N1} = g_{N3} = 0$.

6.3. The Poincaré map

The system has four degrees of freedom, which sets up an eight-dimensional state space $(\mathbf{q}, \dot{\mathbf{q}}) \in \mathbb{R}^8$. However, the accelerations $\ddot{\mathbf{q}}$ are only dependent on $\mathbf{z} = (y_S, \varphi_S, \varphi_B, \dot{\mathbf{q}}) \in \mathbb{R}^7$ and not on the displacement x_S. By a periodic solution of the system, we mean periodic motion of the seven states $\mathbf{z}$. The system allows for a one-dimensional Poincaré map due to the fact that multiple contacts can be closed during the same time interval. We define the section Σ

$$\Sigma = \{\mathbf{z} \in \mathbb{R}^7 \mid g_{N1} = g_{N3} = \dot{g}_{N1} = \dot{g}_{N3} = \dot{g}_{T1} = 0 \wedge \varphi_S = \varphi_S^{r3}\}. \tag{122}$$

For a state $\mathbf{z} \in \Sigma$, the only unknown is the velocity $\dot{\varphi}_S$. From a state $\mathbf{z} \in \Sigma$ with $\dot{\varphi}_S = \dot{\varphi}_{S_k}$, a solution evolves which may return to Σ. The return value of $\dot{\varphi}_S$ on Σ is denoted by $\dot{\varphi}_{S_{k+1}}$. We define the one-dimensional first return map $P : \Sigma \to \Sigma$ as

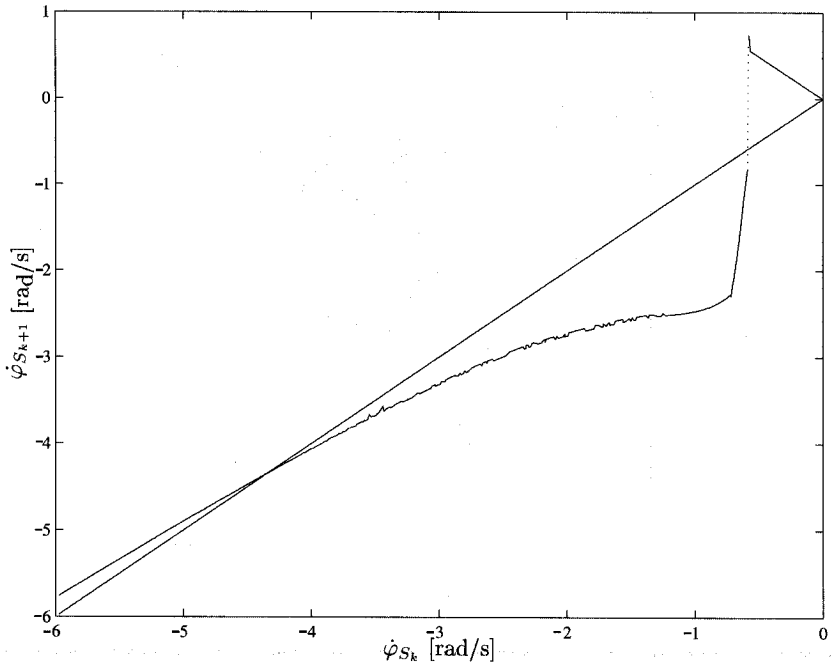

Figure 27. Poincaré map of the waddling duck ($\varphi_R = \frac{\pi}{20}$).

$$\dot{\varphi}_{S_{k+1}} = P(\dot{\varphi}_{S_k}). \tag{123}$$

Periodic solutions and equilibria, which pass the section Σ, are fixed points of P, i.e. they are regular crossings of the map P with the diagonal $\dot{\varphi}_{S_k} = \dot{\varphi}_{S_{k+1}}$. The section Σ has been chosen such that the stable equilibrium resting on the front leg is located on Σ and will therefore appear as a fixed point of P at $\dot{\varphi}_S = 0$.

The Poincaré map P has been calculated for $\varphi_R = \frac{\pi}{20}$ and is shown in Figure 27. The stable periodic solution, which has been discussed earlier and is depicted in Figure 23, appears as a fixed point of P at $\dot{\varphi}_S = -4.3$. The fixed point at $\dot{\varphi}_S = 0$ is, of course, the stable equilibrium. A discontinuity of the map can be observed at $\dot{\varphi}_S = -0.57$ which crosses the diagonal of the map. Solutions starting with $\dot{\varphi}_S > -0.57$ remain resting on the front leg with $g_{N1} = g_{N3} = 0$ for all t, i.e. the solutions converge towards the stable equilibrium point. Solutions starting with $\dot{\varphi}_S < -0.57$ roll at a certain time instant on the rear leg, which opens contacts 1 and 3. Those solutions converge towards the stable periodic solution. The solutions on either side of the discontinuity are therefore structurally different, which causes a discontinuity with respect to the initial condition.

7. CONCLUSIONS

Models of the tumbling toy and the waddling duck have been presented and different aspects of the non-smooth dynamics of these systems have been investigated. The woodpecker toy has already been modeled and studied in Glocker (1995) and Pfeiffer and Glocker (1996), but new results have been obtained on the bifurcation behavior in the present paper. The analysis of the toys is, of course, not complete because many other parameters can be varied. Also, the possibly chaotic behavior of the systems was not studied.

All three toys are higher-dimensional systems with three or four degrees of freedom with unilateral constraints. Still, a one-dimensional map can be obtained for each of the systems by making use of the unilateral characteristic of the systems. The unilateral characteristic of the systems complicates the dynamical behavior of the systems on the one hand, but allows for a one-dimensional map on the other hand, which facilitates the analysis. Smoothing of the non-smooth models would not only yield very stiff differential equations but would also not allow for a one-dimensional map.

A one-dimensional map can, in general, not be obtained. Another disadvantage of one-dimensional mappings is that periodic solutions and equilibria can exist which do not have an intersection point with the Poincaré section. Bifurcation diagrams are therefore usually constructed by continuation techniques (based on a shooting method or other periodic solution solver), which follow branches of periodic solutions or equilibria. Continuation methods have the advantage of being more generally applicable, but have the disadvantage of following a branch locally. If the numerical continuation of a branch of a non-smooth system becomes stuck at a non-conventional bifurcation point, then there is no means to proceed with the continuation because there is no general bifurcation theory available for non-smooth systems. Islands of periodic solutions, or unexpected branches emanating from non-conventional bifurcation points, may be missed by continuation techniques. The analysis by a one-dimensional map is, although not generally applicable, more robust to those problems and gives also more insight into the way the bifurcation is created. The insight in non-conventional bifurcations of non-smooth systems, obtained by analysis of one-dimensional mappings, might eventually be used for the improvement of continuation techniques for non-smooth systems.

Some conclusions about bifurcations in systems with impact and friction can be drawn from the analysis of the three studied systems. A discontinuity in the map is due to a discontinuity with respect to the initial condition. It appears that discontinuous crossings of the map with the diagonal, being due to a topological change of the solution, can exist for systems with unilateral constraints. The coalescence of a branch of periodic solutions with a branch of discontinuity crossings of this type gives rise to a non-conventional bifurcation. A major problem is that a discontinuity in the map can be misinterpreted as being due to the non-smoothness of the system. At least three different mechanisms for discontinuity with respect to initial condition have to be distinguished:

1. *Topological change of the solution (with uniqueness of solutions).* Variation of the initial condition can cause the solution to change its topology, i.e. the order and type of smooth phases. For instance:
   - a change in the order of two subsequent impacts (e.g. the woodpecker toy);
   - an interchange of activity of an active and a passive contact (e.g. the waddling duck).

Note that both examples require a system with multiple contacts.

2. *Non-uniqueness of the solution.* The map becomes multiple valued when the solution is non-unique, for instance for the stick–slip system in Leine et al. (2000) (Section 6.6). The non-uniqueness is in this example due to the friction characteristic with a maximal static friction being unequal to the dynamic friction for zero relative velocity.[4]
3. *Separatrix of a saddle.* Two adjacent initial conditions on different sides of a separatrix will diverge after passing the saddle point. This causes a discontinuity with respect to the initial condition, for instance for the tumbling toy with the homoclinic bifurcation point.

The first two mechanisms can only occur in non-smooth systems and can cause non-conventional bifurcations, whereas the third mechanism can also occur in a smooth system and will yield a conventional bifurcation. We could argue whether the non-uniqueness of the solution is also a topological change of the solution. The first mechanism, however, yields a discontinuous single-valued map whereas the second mechanism yields a multiple-valued map, which is essentially different. Other mechanisms for discontinuity with respect to initial conditions might very well exist, such as loss of existence of solutions.

The stability and bifurcation behavior of periodic solutions of Filippov systems was studied in Leine et al. (2000). It was conjectured and made plausible that the existence and type of bifurcation in the Filippov type of systems is fully determined by the jumps in the Floquet multipliers. Floquet multipliers give information about the slope of the map. In the present paper, we study bifurcations in systems with impact and friction, which no longer belong to the class of Filippov systems. The one-dimensional maps of systems with impact are generally discontinuous whereas they are non-smooth but continuous for Filippov systems. Thus, it cannot be expected that the stability and bifurcation behavior of systems with impact can be retrieved from the Floquet multipliers alone, as the Floquet multipliers do not give information about the discontinuity of the map. Systems with impact are therefore intrinsically more difficult than Filippov systems. Impacting systems with a single contact point can be transformed to a Filippov system by the non-smooth Zhuravlev–Ivanov transformation (Brogliato, 1999; Ivanov, 1996). The results of discontinuous bifurcations of Filippov systems can therefore be used as a stepping stone to bifurcations in impacting system. However, the Zhuravlev–Ivanov transformation is restricted to a single contact. Discontinuity with respect to initial conditions due to a change of order of two events can therefore not be studied with this transformation because it implies multiple contact points.

One of the peculiarities of systems with impact is the existence of discontinuity crossings with the diagonal (being due to the non-smoothness of the system). Branches of discontinuity crossings seem to connect branches of stable and unstable periodic solutions and are therefore of interest as new "objects" in the bifurcation diagram. Discontinuity crossings appear in a one-dimensional map. It would be of interest to know whether such "objects" can also be found with a shooting type of algorithm.

The analysis of the three toys has shown some aspects of the bifurcation behavior of systems with impact and friction. The fact that they are multiple-degree-of-freedom systems, which still allow for a one-dimensional map, makes them excellent candidates to be benchmark systems for the analysis of bifurcation in systems with impact and friction.

NOTES

1. Mathematically more correct is to consider the impact as a singleton, i.e. a point in time, and the equation of motion as a measure differential equation, which is beyond the scope of this paper; see Glocker (2000) and Moreau (1988).
2. The word 'homoclinic' at this point is not completely satisfactory because the solution at the bifurcation point travels from one saddle point to the next and is therefore a set of heteroclinic connections. However, we can speak of a homoclinic connection when we consider $\varphi_S \bmod \pi$.
3. To be more precise, we should say that there exists a set of similar equilibria because this type of equilibrium exists for all values of x_S. Each set of similar equilibria will be denoted as an equilibrium in the following for convenience.
4. The friction model contains some hysteresis behavior where the difference between loading and unloading has shrunk to one point (Glocker, 2000; 2001).

REFERENCES

Begley, C. J. and Virgin L. N., 1997, "A detailed study of the low-frequency periodic behavior of a dry friction oscillator," *Journal of Dynamic Systems, Measurement, and Control* **119**, 491–497.

Beitelschmidt, M., 1999, *Reibstöße in Mehrkörpersystemen*, Fortschr.-Ber. VDI Reihe 11, Nr. 275, VDI Verlag, Düsseldorf.

Blazejczyk-Okolewska, B. and Kapitaniak, T., 1996, "Dynamics of Impact Oscillator with Dry Friction," *Chaos, Solitons and Fractals* **7**(9), 1455–1459.

Brogliato, B., 1999, *Nonsmooth Mechanics*, Springer, London.

Canudas de Wit, C., Olsson, H., Åström, K. J., and Lipschinsky, P., 1995, "A new model for control of systems with friction," *IEEE Transactions on Automatic Control* **40**(3), 419–425.

Cottle, R. W. and Dantzig, G. B., 1968, "Complementary pivot theory of mathematical programming," *Linear Algebra and its Applications* **1**, 103–125.

Dankowicz, H. and Nordmark, A. B., 2000, "On the origin and bifurcations of stick–slip oscillations," *Physica* D **136**(3–4), 280–302.

di Bernardo, M., Feigin, M. I., Hogan, S. J., and Homer, M. E., 1999, "Local analysis of C-bifurcations in n-dimensional piecewise-smooth dynamical systems," *Chaos, Solitons and Fractals* **10**(11), 1881–1908.

Foale, S. and Bishop, R., 1994, "Bifurcations in impact oscillations," *Nonlinear Dynamics* **6**, 285–299.

Galvanetto, U. and Knudsen, C., 1997, "Event maps in a stick–slip system," *Nonlinear Dynamics* **13**(2), 99–115.

Glocker, Ch., 1995, *Dynamik von Starrkörpersystemen mit Reibung und Stößen*, Fortschr.-Ber. VDI Reihe 18, Nr. 182, VDI Verlag, Düsseldorf.

Glocker, Ch., 2000, "Scalar force potentials in rigid multibody systems" in *Multibody Dynamics with Unilateral Contacts*, eds. F. Pfeiffer, Ch. Glocker, CISM Courses and Lectures Vol. 421, pp. 69–146, Springer, Wien.

Glocker, Ch., 2001, *Set-Valued Force Laws, Dynamics of Non-Smooth Systems*, Springer-Verlag, Berlin.

Guckenheimer, J., and Holmes, P., 1983, *Nonlinear Oscillations, Dynamical Systems, and Bifurcations of Vector Fields*, Vol. 42, Springer-Verlag, New York.

Ivanov, A. P., 1996, "Bifurcations in Impact Systems," *Chaos, Solitons and Fractals* **7**(10), 1615–1634.

Leine, R. I. and Van Campen, D. H., 1999, "Fold bifurcations in discontinuous systems," in *Proceedings of DETC 99 ASME Design Engineering Technical Conferences*, September 12–15, Las Vegas, CD-ROM, DETC99/VIB-8034.

Leine, R. I. and Van Campen, D. H., 2000, "Discontinuous bifurcations of periodic solutions," accepted for publication in *Mathematical Modelling of Nonlinear Systems*.

Leine, R. I., Van Campen, D. H., and Van de Vrande, B. L., 2000, "Bifurcations in nonlinear discontinuous systems," *Nonlinear Dynamics* **23**(2), 105–164.

Leine, R. I., 2000, *Bifurcations in Discontinuous Mechanical Systems of Filippov-Type.* Ph.D. thesis, Eindhoven University of Technology, The Netherlands.

Meijaard, J. P., 1996, "A mechanism for the onset of chaos in mechanical systems with motion-limiting stops," *Chaos, Solitons and Fractals* **7**(10), 1649–1658.

Moreau, J. J., 1988, "Unilateral contact and dry friction in finite freedom dynamics" in *Non-Smooth Mechanics and Applications*, J. J. Moreau, and P. D. Panagiotopoulos, eds. CISM Courses and Lectures Vol. 302, pp. 1–82, Springer, Wien.

Natsiavas, S. and Gonzalez, H., 1992, "Vibration of harmonically excited oscillators with asymmetric constraints," *ASME Journal of Applied Mechanics* **59**, 284–290.

Nordmark, A. B., 1997, "Universal limit mapping in grazing bifurcations," *Physical Review* E **55**(1), 266–270.

Peterka, F., 1996, "Bifurcations and Transition Phenomena in an Impact Oscillator," *Chaos, Solitons and Fractals* **7**(10), 1635–1647.

Pfeiffer, F., 1984, "Mechanische Systeme mit unstetigen Übergängen," *Ingenieur-Archiv* **54**, 232–240.

Pfeiffer, F., 1991, "Dynamical systems with time-varying or unsteady structure," *Zeitschrift für Angewandte Mathematik und Mechanik* **71**(4), T6–T22.

Pfeiffer, F. and Glocker, Ch., 1996, *Multibody Dynamics with Unilateral Contacts*, Wiley, New York.

Popp, K., Hinrichs, N., and Oestreich, M., 1995, "Dynamical behaviour of a friction oscillator with simultaneous self and external excitation," in *Sādhāna: Academy Proceedings in Engineering Sciences*, Indian Academy of Sciences, Banglore, India, Part 2–4,Vol. 20, pp. 627–654.

Roßmann, T., 1998, *Eine Laufmachine für Rohre*, Fortschr.-Ber. VDI Reihe 8, Nr. 732, VDI Verlag, Düsseldorf.

Van de Vrande, B. L., Van Campen, D. H., and De Kraker, A., 1999, "An approximate analysis of dry-friction-induced stick–slip vibrations by a smoothing procedure," *Nonlinear Dynamics* **19**(2), 157–169.

Wiercigroch, M., 1996, "On modelling discontinuities in dynamic systems," *Machine Vibration* **5**, 112–119.

Yoshitake, Y. and Sueoka, A., 2000, "Forced self-exited vibration accompanied by dry friction," in *Applied Nonlinear Dynamics and Chaos of Mechanical Systems with Discontinuities*, M. Wiercigroch and A. de Kraker, eds. World Scientific, Singapore.